Atmospheric Reaction of Hydrazine Plus Hydroxyl Radical. I. Reliable Pathways

Hamed Douroudgari (douroudgari@znu.ac.ir)
University of Zanjan
Morteza Vahedpour
University of Zanjan
Fahime Khouini
University of Zanjan

Research Article

Keywords: hydrazine oxidation, quantum chemical methods, addition/elimination reactions, barrierless pathways

Posted Date: March 24th, 2021

DOI: https://doi.org/10.21203/rs.3.rs-342563/v1

Atmospheric reaction of hydrazine plus hydroxyl radical.

I. Reliable pathways

Hamed Douroudgari*, Morteza Vahedpour*, Fahime Khouini

Department of Chemistry, University of Zanjan, PO Box 38791-45371, Zanjan, Iran

E-mail: douroudgari@znu.ac.ir

E-mail: vahed@znu.ac.ir

Abstract

Understanding the mechanism of hydrazine oxidation reaction by OH radical accompanied by the rate constants of all possible pathways is important. They are key parameters to explain the fate of hydrazine in the atmosphere. To reach the mentioned parameters, higher-level calculations by using quantum chemical methods have been implemented comprehensively for reliable channels such as H-abstraction, S_N2, and addition/elimination reactions. To estimate the barrier energies of H-abstraction channels accurately, large numbers of the CCSD(T)/X calculations (where X denotes the augmented Dunning and Pople double zeta or triple zeta basis sets) have been applied to the optimized geometries of the MP2/aug-cc-pVTZ, MP2/maug-cc-pVTZ, and M062X/maug-cc-pVTZ levels. Contributions of excited states on the computed potential energy surface have been considered by the MR-MP2 (multi-reference) method in conjunction with the large augmented quadruple zeta, aug-cc-pVQZ, basis sets. The direct dynamic calculations have been carried out using the accurate energies of the CCSD(T) method and the partition functions of the second-order MØller-Plesset perturbation theory, and also by the validated M06-2X method with the aug-cc-pVTZ, and maug-cc-pVTZ basis sets. Finally, The VTST and TST theories have been used to calculate the temperature dependence of rate constants of the considered pathways. Also, the pressure-dependent rate constants of the barrierless pathways have been investigated by the strong collision master equation/RRKM theory.

Introduction

Hydrazine has three structural conformers: *s-cis* (C_{2h}), *anti* (C_{2v}), and *gauche* (C_2). The gauche-conformer is the most stable, and the anti-conformer is more stable than the *cis*. In industry, hydrazine and its derivatives have many applications such as polymerization initiators, boiler water treatment, dyes[1-5], and corrosion inhibitors for steel in contact with hot water[6-8]. Also, hydrazine plays an important role in the production of organic compounds[9]. The International Agency for Research on Cancer (IARC) and American Conference of Governmental Industrial Hygienists (ACGIH) take into account hydrazine as a carcinogenic substance with an unknown relevance for both animals and humans[10]. In unsymmetrical structures, the fuels containing hydrazine, methyl hydrazine, and dimethylhydrazine compounds are high-energy and have special applications such as fuels of rockets and spacecraft. All of them are crudely toxic[11-14]. Usually, some of the oxidizers are added to hydrazine fuels for high performance. The most common oxidizers are dinitrogen tetroxide (NTO) and inhibited red fuming nitric acid (IRFNA).[15-17] Because decomposition of NTO and nitric acid can produce hydroxyl radicals and nitrogen dioxide, the reactions of hydrazine with these species are important in designing rockets[18]. Knowledge of hydrazine oxidation reactions has some advantages. The most important advantage is the development of the gelled hypergolic propellant (GHP) [19]. In the atmosphere, the complete decomposition of hydrazine with reactive species is probable[20]. A few numbers of experimental studies[21-24] and only one theoretical investigation[25] have been performed previously on the mechanisms and kinetics of the $N_2H_4 + OH$ reaction in the second-order form. The obtained results have been shown that hydrogen abstraction via hydroxyl radical is the main reaction pathway at temperatures lower than 700 K.

$$N_2H_4 + OH \rightarrow N_2H_3 + H_2O \qquad (1)$$

Also, the main reaction of hydrazine with O_3 as other important atmospheric species is as follows: [12,26]

$$N_2H_4 + O_3 \rightarrow N_2H_3 + OH + O_2 \qquad (2)$$

Vaghjiani[21]experimentally investigated the gas-phase rate constant of OH reaction with the hydrazine in the temperature range of 232-374 K and reported an expression as $k=(1.25\pm0.19) \times 10^{-11}\exp[(315\pm55)/T]$ cm^3 $molecule^{-1}$ s^{-1}. This expression has a weak temperature dependence. In another

study, he reported another Arrhenius expression as $k=(2.17\pm0.39) \times 10^{-11}\exp[(160\pm30)/T]$ cm^3 $molecule^{-1}$ s^{-1} at the 232–637 K temperature range. Also, he recommended that OH radicals can not be added to one center of diamine in low temperatures, and thus the reaction does not progress by rapid dissociation of the intermediate into products[22]. Harris *et al.*[23] measured the rate constants of the title reaction by using photolysis-resonance fluorescence in the 298-424 K temperature range. They found a rate expression as $k=4.40 \times 10^{-11}\exp[(116\pm176)/T]$ cm^3 $molecule^{-1}$ s^{-1}. Hack *et al.*[24] investigated the rate of hydrazine with hydroxyl radical, $OH + N_2H_4 \rightarrow$ products, in an isothermal flow reactor with helium flow as the carrier gas. The overall rate constant was $k(298.15)=2.20 \times 10^{-11}$ cm^3 $molecule^{-1}$ sec^{-1} at room temperature and pressure around 2 Torr. The reaction of N_2H_4 + OH was studied by Tang and *et al.*[25] theoretically. The calculated rate expressions over 200-3000 K temperature range were $k_1=7.79 \times 10^{-18}T^{1.93}\exp(-1258.5/T)$ and $k_2=1.28 \times 10^{-18}T^{2.37}\exp(-1049.3/T)$ cm^3 $molecule^{-1}$ sec^{-1} for H-abstraction reaction (generation of the N_2H_3 plus H_2O products) and S_N2 reaction (production of the NH_2 plus H_2NOH adducts), respectively. For the N_2H_4 reactant, the following results show that there is an inconsistency between the reported optimized geometry by Tang et al. and the original geometry of this reactant at the B3lyp/6-311g(d,p) level. On one hand, the B3LYP/6-311G(d,p) and the CCSD(T)/6-311++G(d,p)//B3LYP/6-311G(d,p) levels are weak computational levels to describe a potential energy surface especially in reactions including small compounds such as the N_2H_4 plus OH reaction[27-30]. On the other hand, the computed relative energies at this level were corrected and found that these levels have no accurate transition structures and energies. In addition, on the basis of our results, there are large discrepancies between the rate constants calculated at the CCSD(T)/6-311++G(d,p)//B3LYP/6-311G(d,p) level and the abovementioned experimental results, so further calculations are needed to resolve the problem. Therefore, it is concluded that higher-level calculations are necessary to compute the saddle points structures and the potential energy surface of the title reaction. It will be discussed in more detail in the result and discussion section.

To the best of our knowledge, there are neither experimental studies at temperatures above 650 K and nor reliable theoretical data obtained by higher-level calculations. In the present work, the hydrazine plus hydroxyl radical reaction channels are investigated using both single reference and multi-reference methods to yield a more accurate potential energy surface, to calculate the exact rate constant for each channel at various temperatures, and to predict more precise thermodynamic parameters. Therefore, the potential energy surface is computed using higher-level methods such as

the CASSCF-MP2 method (the multi-reference MØller-Plesset second-order perturbation theory), the CCSD(T) method (the coupled-cluster theory), and the MP2 method (the single reference MØller-Plesset second-order perturbation theory) in connection with various basis sets to obtain more accurate and complete treatment of the N_2H_4 + OH reaction pathways. Furthermore, the other main objectives of this study are fully and completely describing the mechanisms of the N_2H_4 + OH reaction comprehensively, and obtaining more accurate theoretical insight into the stationary points of computed PES using the topological theory of atoms in molecules (AIM) and NBO analysis. The rate constant calculations are carried out for all reaction pathways at the high-pressure limits by using transition state (TST) and variational transition state VTST theories, and at the low- pressure limit and falloff regime by the strong collision master equation Rice-Ramsperger-Kassel-Marcus (RRKM) theory.

Computational methods

The UMP2[31] and very popular density functional method, UB3LYP[32,33], with the 6-311++G (3df, 3pd), maug-cc-pVTZ[34], aug-cc-pVTZ, and aug-cc-pVQZ[35] basis sets and also some other basis sets were applied to geometry optimization of all stationary points in doublet state. Due to serious shortcomings of the most popular density functional method, B3LYP, in determining barrier heights and so kinetics of reactions, especially in reactions containing hydrogen shifts, we have used the UM06-2X[36,37] method. This method is a highly parameterized meta hybrid density functional method and has reasonable results for specifying reaction kinetics.

The harmonic vibrational frequencies were computed by using the abovementioned methods and basis sets to determine the nature of all stationary points, including prereactive collision complexes (MCr), product complexes (MCp), and transition states (TS). In the whole paper, It was used the maTZ, aTZ, and aQZ for shorthand notations of the maug-cc-pVTZ[34], aug-cc-pVTZ, and aug-cc-pVQZ[35] basis sets, respectively. All of the structures concerning the minimum-energy points on the considered PES have only real frequencies, and all of the saddle point structures have just one imaginary frequency.

The zero-point vibrational energies were included in the calculated relative energies. Moreover, to evaluate the connectivity of all stationary points and also to compute the minimum-energy paths, we

carried out the intrinsic reaction coordinate (IRC)[38,39] calculations (MEP) for all saddle point structures using the MP2 and M06-2X methods.

To estimate the barrier heights of the title reaction more precisely, a dual-level methodology was used similar to previous reactions of hydrazine with atomic oxygen simulated in the atmospheric conditions[40-42]. Thus, the CCS(T)/CBS//MP2/aTZ level was chosen. Because (a) (in the mentioned studies) it has been proved that the CCS(T)/CBS level has excellent results in energy prediction (b) the MP2 method along with a large basis set has better results than small basis sets[43] for geometry optimization of all stationary points containing hydrogen bonds[44] like the N_2H_4 + OH reaction. Therefore, we used the geometries obtained at the MP2/aTZ level for the CCSD(T)/CBS calculations. For constructing the CCSD(T)/CBS level, the results of the CCSD(T)/aQZ//UMP2/aTZ and CCSD(T)/aTZ//UMP2/aTZ levels were extrapolated to the complete basis set, CBS, limit using the suggested method by Halkier et al. [45]. To evaluate the effects of excited states on the potential energy surface, the multi-reference MØller-Plesset second-order perturbation method, MR-MP2[46,47], in connection with the augmented correlation-consistent polarized quadruple-zeta, aug-cc-pVQZ, basis set were implemented on the structures obtained at the UMP2/aTZ and UM06-2X/aTZ levels. The T1 diagnostic[48,49] values were calculated at CCSD(T)/Y level (Y= several basis sets of the Dunning and Pople types) for confirming the importance of higher-level calculations to the electronic structures of all species. If T1 diagnostic values are greater than 0.045 for both closed-shell and open-shell systems, higher-level calculations are needed for investigating systems [50-52]. The same value for the Largest amplitudes is 0.2, but our results are below 0.2 (0.045) except TS1b (see Table S32). This is obvious for TS1b because we found the structure of TS1b through the scan option as mentioned in the *H_2NOH + NH_2 formation channels* section. Also, according to the proposed PES, the path containing TS1b has a very small contribution to hydrazine degradation due to having a transition state with a high energy barrier (see Figure 1). And this path is not observed in experimental studies. This is only a theoretical pathway and does not affect the total rate of hydrazine degradation.

To explore deeper insight about the reaction mechanisms, the bonds taking part in reactions were analyzed based on the natural bond orbital, NBO, and the atoms in molecule, AIM, analyses at the UMP2/aTZ level. Also, the thermodynamic parameters of the predicted adducts were computed in the temperature range of 200-1200 K at the M06-2X/aQZ and MP2/aTZ levels. The topological analyses of the wave functions were implemented by the AIM2000[53] program. Gaussian 09 package program

was executed for optimization and electronic structure calculations of all stationary points[54]. All images of molecular structures were created using the GaussView 5.0.8 software[55].

Rate constant calculations

All rate constants were calculated at the high-pressure limit using the transition state (TST) theory[56] as follows:

$$k(T) = \kappa \frac{k_B T}{h} \left(\frac{Q_{TS}^{\neq,IG}}{Q_{N_2H_4}^{IG} Q_{OH}^{IG}}\right) \exp\left(-\frac{\Delta^{\neq} E^{el}}{k_B T}\right) \qquad (1)$$

where κ is tunneling factor. Q_X^{IG} is the partition function of X component that is assumed to be an ideal gas. k_B and T are the Boltzmann constant and temperature, respectively. h is the Planck constant. $\Delta^{\neq} E^{el}$ is the difference of electronic energies between a transition state and the sum of reactants. Also, the variational effects on the reaction rate were implemented by the variational transition state theory (VTST)[57]. For all elementary bimolecular reactions, the high-pressure limit rate constants were computed by the Gpop program[58]. The rate constants at the low-pressure limit and the falloff regime were calculated using the strong collision master equation/Rice-Ramsperger-Kassel-Marcus (RRKM) theory by the Ssumes program[59].

The main channels of the reaction in this work are hydrogen shift. Thereby, the exact quantum tunneling correction factor is necessary. The quantum tunneling correction factor was calculated at the UMP2/aTZ and M06-2X/maTZ levels. For the mentioned correction, the second-order correction of Shavitt[60] was used as follows:

$$k_i(T) = 1 - \left(\frac{1}{24}\right)\left(\frac{h\upsilon_{im}c}{k_B T}\right)^2 \left(\frac{1 + k_B T}{E_0}\right)$$

where k_B is Boltzmann constant, ν_{im} is imaginary frequency of a transition state, c is the speed of light, T is temperature, and E_0 is barrier height that may correct by zero-point energy for the considering reaction (E_{TS1} - E_R).

As the authors of the UM06-2X[36,37] method have recommended this method has excellent performance for main group thermochemistry, noncovalent interactions, and kinetics. Therefore, the rate constants of the N_2H_4 + OH reaction were computed at the M06-2X/maTZ level.

Results and discussion

In the following sections, for the N_2H_4 + OH reaction, the potential energy surface, rate constants of all reliable pathways at low, intermediate, and high pressures, and also thermodynamic data are discussed using different computational methods. Finally, the fate of hydrazine is studied in different heights of the atmosphere. Also, we use the same notation for stationary points as Tang et al. to simplify the PES following in both works.

Potential energy surface

The potential energy diagram of the N_2H_4 + OH reaction is depicted in Figure 1. The relative energies of this figure are computed at the CCSD(T)/CBS level. The selected geometrical parameters of all species in the proposed pathways are shown in Figure 2. Also, the selected bond lengths of key saddle points are listed in Tables 1, S1, and S2 (see supporting information). The unscaled vibrational frequencies of stationary points are summarized in Table S3. The energetic parameters of all stationary points computed at the CCSD(T)/CBS level are given in Table 2. Also, these parameters are calculated in several methods and various basis sets and collected in Tables S4-S6 (see supporting information). The thermodynamic variables of all predicted adducts in the temperature range of 200-1200 K are calculated at both the UM06-2X/aQZ and UMP2/aTZ levels and collected in Tables 4 and S31. The temperature dependence of rate constants for all elementary reactions is calculated by TST and VTST theories. The obtained results are tabulated in Tables 3a and 3b, and Tables S7-S28 in additional information. The pressure-dependent rate constants for all H-abstraction channels are listed in Table S29.

Reaction entrance channels

Like many gas-phase reactions, the hydrazine reactions with hydroxyl radical begin with pre-reactive collision complexes. In this work, three pre-reaction complexes are predicted and named by MCr1a, MCr1b, and MCr2. The complex MCr1a is a mirror image of MCr1b. Therefore, the electronic

structure of MCr1a is the same as MCr1b. Also, the structure of MCr1a (or MCr1b) including N_2H_4 and OH is associated with the formation of hydrogen-bond. So, they are more stable than MCr2. In MCr2, the hydroxyl radical moiety has a covalent bond with the lone pair electrons of the nitrogen atom of N_2H_4 moiety. This is a reason to increase the length of the H1-N2 bond in MCr2 in comparison with the corresponding bond in isolated hydrazine. The covalent interaction in MCr2 caused the HOMO α and β orbitals (in unrestricted formalism) to have higher energy than the HOMO orbitals in MCr1a and MCr1b. In the MCr2 complex, the difference between the absolute energies of the LUMO α and β orbitals is large. So, it is unstable complex in the doublet state. In MCr2, the covalent nature of the newly formed bond (O1-N2) with a length of 1.389 Å is confirmed by AIM analysis [ρ (r_{bcp}) =0.3454 e bohr^{-3} and $\nabla^2\rho(r_{bcp})$ = -3.8432 e bohr^{-5}]. Also, an NBO analysis confirms that the O1-N2 bond in MCr2 is a sigma (σ) type with covalent nature. Also, the contributions of the involved orbitals in σ (O1-N2) bond are as follows:

(BD(N2-O6))= 0.6883 ($sp^{3.51}$) N2 + 0.7254 ($sp^{4.44}$) O6

In MCr1a and MCr1b, the hydrazine fragment is a hydrogen bond acceptor and the OH fragment is a hydrogen bond donor. The AIM parameters of the N2…OH interaction in MCr1a are ρ (r_{bcp}) = 0.0366 e bohr^{-3} and $\nabla^2\rho$ ($_{bcp}$) = 0.0732 e bBohr^5 that confirms the existence of a hydrogen bond. In this complex, the amounts of the standard enthalpy and Gibbs free energy at the M06-2X/aTZ (and MP2/aTZ) level is 7.01 (6.76) and 0.92 (0.91) kcal/mol, respectively, in comparison with the original reactants at room temperature. For MCr2, the mentioned thermodynamic parameters are 42.93 (40.45) and 52.72 (50.24) kcal/mol, respectively.

Firstly, in the following sections, the H abstraction (barrier-less) reaction channels will be discussed. Secondly, hydroxyl radical addition to the N site of hydrazine will be investigated. Finally, the S_N2 reaction (OH replacement with a hydrogen atom of hydrazine) will be argued.

N_2H_3 + H_2O formation channels

The H abstraction channels start with MCr1a and MCr1b complexes. The relative energy of MCr1a is -7.88 kcal/mol at the CCSD(T)/CBS level. The H abstraction reactions are summarized as follows:

1) N_2H_4 + OH→ MCr1a→TS2→MCp1→ P1(H_2NNH + H_2O) (Path 1)

2) $N_2H_4 + OH \rightarrow MCr1b \rightarrow TS3 \rightarrow MCp2 \rightarrow P1(H_2NNH + H_2O)$ (Path 2)

These paths were studied by Tang and et al. at the CCSD(T)/6-311++G(d,p)//B3LYP/6-311G(d,p) + ZPE level and the reported relative energies for TS2 and TS3 were -1.67 and 0.41 kcal/mol, respectively.

We recomputed their suggested pathways at the same level and geometries. Our results show that the relative energies with including ZPE (and without including ZPE) for TS2 and TS3 are 0.38 (-0.12) and 2.65 (1.58) kcal/mol (compared with -1.67 and 0.43 kcal/mol), respectively. The discrepancy of our results and Tang work may be related to the optimized geometry of the N_2H_4 molecule at the B3LYP/6-311G(d,p) level. In Tang et al. study, the geometrical parameters of the N_2H_4 molecule were 1.487 Å for N-N bond and 1.020 Å for N-H bond, but our computed lengths are 1.435 Å and 1.018 Å for that bonds, respectively. For other species, the recomputed geometrical parameters at the mentioned level are the same as Tang et al. The T1 diagnostic values for some species calculated at the CCSD(T) method with different basis sets are in the range of 0.025-0.038. These values show that the higher-level calculations like the CCSD(T)/CBS//MP2/aTZ are important for a more accurate prediction of the energies and geometries of all stationary points. Therefore, the CCSD(T)/6-311++G(d,p)//B3LYP/6-311G(d,p) level is inadequate due to having small basis set to describe the mechanism and PES of the title reaction.

Based on the following results, for the H-abstraction saddle points, two different formalisms have different structures. In the DFT methods such as the B3LYP and M06-2X using several basis sets, the obtained structures are similar to the reactants, which are named early transition states. The ab initio methods such as the CASSCF and MP2 show that the structures of TS2 and TS3 are similar to neither reactants nor products. These transition states are called case transition states. For these reasons, we investigate the barrier heights and the rate constants using both formalisms. Using the ab initio methods, the MEP calculations show that TS2 and TS3 connect to MCr1a. The H abstraction reactions in paths 1 and 2 occur via TS2 and TS3, respectively. The IRC calculations verify that the formation of the complex products MCp1 and MCp2 is possible in the gas phase. The relative energies of MCp1 and MCp2 are -44.45 and -44.26 kcal/mol at the CCSD(T)/CBS level, respectively. The barrier energies (and relative energies) of TS2 and TS3 at the CCSD(T)/CBS level are 4.80 (-3.08) and 5.49 (-2.39) kcal/mol. Also, the computed barrier energies and relative energies of TS2 and TS3 at different

methods and basis sets are listed in Table S5. The results show that the transition state structures and energies are sensitive to the applied methods and basis sets. It should be noted that the bond length and features of the OH and the shifting hydrogen of hydrazine in TS2 and TS3 are crucial. In MCr1a, the atoms H7 and O6 with a length of 2.76 Å have no interaction with each other. The corresponding bond length (H7-O6= 1.464 Å) in TS2 is shorter than MCr1a. Also, the NBO outputs show that the mentioned bond in MCp1 and MCp2 is a covalent bond:

MCp1 (σ BD (H7-O6)) = 0.8712 ($sp^{2.72}$) O6 + 0.4909 ($s^{0.99}$) H7

In MCp1, the N-N bond length is decreased compared with that bond in MCr1a. This change causes to make a bond with the π character in nature and agrees with the following atomic hybridization:

MCp1 (σBD (N1-N2)) = 0.6702 ($sp^{2.50}$) N + 0.7422 ($sp^{1.83}$) N2

(N1 occupies 44.91%, which involves 28.45% s orbital and 70.98% p orbital; N2 occupies 55.09%, which involves 35.19% s orbital and 64.44% p orbital.)

The electronic charge density of the ring critical point (RCP) for MCp1 and MCp2 is ρ (r_{rcp}) = 0.0129, and 0.0128 e $bohr^{-3}$, respectively. Also, the Laplacian of the charge density for that rings is $\nabla^2\rho(r_{rcp})$ =0.0706 and 0.0714 e $bohr^{-5}$, respectively. The variation of the electronic charge density and its Laplacian confirms the hydrogen shift in path 1. Finally, the complex products, MCp1 and MCp2, by barrier-less processes release to the N_2H_3 and H_2O adducts.

$H_2NOH + NH_2$ formation channels

The $H_2NOH + NH_2$ generation pathways (S_N2 and addition/elimination reactions) are summarized as follows:

3) $N_2H_4 + OH \rightarrow$ MCr1b$\rightarrow$ TS1$\rightarrow$ MCp3a$\rightarrow$ P2($H_2NOH + NH_2$) (Path 3)
4) $N_2H_4 + OH \rightarrow$ MCr2$\rightarrow$ TS1b$\rightarrow$ MCp3b$\rightarrow$ P2($H_2NOH + NH_2$) (Path 4)

Also, in the next section, we introduce another path for the production of P2 products. The third pathway begins with MCr1b pre-reactive complex, and the fourth pathway starts with MCr2. The substitution reaction between OH and NH_2 fragments is an S_N2 reaction similar to the organic

reactions, occurring simultaneously. The NBO and MEP calculations confirm the S_N2 substitution reaction. In this process, the hydroxyl radical is approaching the hydrazine molecule from behind, and the NH_2 functional group is separating from the front side.

TS1 (BD (O6-N2)) = 0.6127 ($sp^{12.35}$) O6 + 0.7903 ($sp^{2.81}$) N2

This NBO analysis shows that the oxygen atom of hydroxyl moiety with $sp^{12.35}$ hybrid orbital in TS1 has a weak covalent bond with non-bonding $sp^{2.81}$ hybrid orbital of the atom N of hydrazine moiety. At the same time, the N-N bond is weaker than the corresponding bond in an isolated hydrazine molecule.

TS1 (BD (N1- N2)) = 0.4925 ($sp^{13.32}$) N1 + 0.8703 ($s^{2.27}$) N2

Tang *et al*. investigated also the substitution reaction between OH and NH_2 moieties. They computed the electronic structure of this path at the CCSD(T)/6-311++G(d,p)//B3LYP/6-311G(d,p) + ZPE level and showed that the OH radical group by surmounting a barrier height of 17.02 kcal/mol replaces to NH_2 moiety. Our calculated relative energy at the CCSD(T)/6-311++G(d,p)//B3LYP/6-311G(d,p) level with (and without) ZPE for that replacement is 21.52 (20.38) kcal/mol. Also, Our computed barrier (and relative) energy for this substitution at the higher level, CCSD(T)/CBS, is 28.28 (20.41) kcal/mol.

MCr2 is an energetic complex. So, it can be decomposed into several adducts. In this research, we investigate the only production of $NH_2OH + NH_2$ adducts. For this purpose, the relax scan option of Gaussian software was used. In MCr2, our calculated barrier energy for the N-N bond cleavage is 13.86 kcal/mol at the CCSD (T)/CBS level leading to produce the $H_2NOH + NH_2$ adducts by passing through TS1b.

H_2NNHOH + H formation channels

H_2NNHOH + H production pathways (S_N2 and addition/elimination reaction) are as follows:

5) $N_2H_4 + OH \rightarrow$ MCr1b $\rightarrow$ TS4 $\rightarrow$ MCp4 $\rightarrow$ P3($H_2NNHOH + H$) (Path 5)
6) $N_2H_4 + OH \rightarrow$ MCr1b $\rightarrow$ TS4 $\rightarrow$ MCp4 $\rightarrow$ TS1c $\rightarrow$ MCp3c $\rightarrow$ P2($H_2NOH + NH_2$) (Path 6)

These pathways begin with MCr1b pre-reactive complex. The substitution reaction between H and OH is also the S_N2 type. The replacement of hydroxyl radical with one hydrogen atom of hydrazine via TS4 happens by overcoming the barrier height of 51.05 kcal/mol at the CCSD(T)/CBS level. The IRC trajectory calculation confirms the production of MCp4 via TS4 through the S_N2 process. The calculated high-pressure limit rate constant shows that the substitution reaction takes place in 700 cm^{-1}. The imaginary frequency of TS4 is 2169 cm^{-1} at the UMP2x/aTZ level. The binding energy of the N-H bond in isolated hydrazine is 89.82 kcal/mol at the CCSD(T)/CBS level (and 88.41 kcal/mol at the UM06-2X/QZ level). So, the barrier energy of TS4 is lower than the binding energy. The binding energy of the N-H bond in hydrazine is the energy difference between two unstable radicals, N_2H_3 and H, and stable hydrazine molecule. On one hand, when the hydrogen atom in TS4 leaves the nitrogen atom of the hydrazine fragment, the N2-H3 bond increases in comparison with the corresponding bond in isolated hydrazine. On the other hand, in the TS4 structure, the hydroxyl radical is approaching the nitrogen atom from behind and forms a weak covalent bond. So, the N-H covalent bond converts to a weak covalent interaction. These interactions are the origin of stability for TS4 fragments compared to N_2H_3 and H free radicals. The NBO and AIM analyses show a weak covalent bond among the non-pair electrons of the atom N2 and hydroxyl radical. Also, the same interaction is observed between the atoms H3 and N2 in TS4 (similar to S_N2 substitution reaction):

TS4 (BD (N2 - H3)) = 0.9142 ($sp^{2.60}$) N2 + 0.4054 ($s^{0.99}$) H3

TS4 (BD (N2 - O6)) = 0.7428 ($sp^{3.00}$) N2 + 0.6695 ($sp^{8.59}$) O6

An NBO analysis of TS4 shows that the $sp^{3.00}$ hybrid orbital of the atom N2 has a weak covalent interaction with the $sp^{8.59}$ hybrid orbital of the atom O6. The $sp^{3.00}$ hybrid orbital of the atom N2 is varied to $sp^{2.60}$. It shows that the p orbital contribution is decreased in the N-H bond during the S_N2 process. The instability of MCp4 is related to the separated hydrogen atom.

The last path is another route for the production of the NH_2OH + NH_2 adducts. After MCp4 generation, MCP3b post reactive complex is created through TS1c by surmounting on the barrier height of 59.91 kcal/mol. This path is long, so kinetically it has less importance compared to the other pathways discussed above.

The high-pressure limit rate constant

The temperature dependence of rate constants for all elementary reactions is obtained via both variational transition state theory (VTST) and transition state theory (TST) for bimolecular reactions. Then, the rate constants are improved by Shavit tunneling correction. To achieve more reliable rate constants, higher-level calculations are performed such as the CCSD(T)/CBS//MP2/aTZ, CCSD(T)/aQZ//MP2/aTZ, CCSD(T)/aTZ//MP2/aTZ, and validated DFT-M06-2X/maTZ levels. Our calculated high-pressure limit rate constants in different levels at the temperature range of 230-3000 K are collected in Tables 3a and 3b, and Tables S7-S28 (see supporting information). From a kinetic point of view, the rate constants for one step elementary reactions are more important. So, in this section, we consider the production pathways of N_2H_3 + OH, NH_2OH + NH_2, and H_2N_2HOH + H products that need to pass just one transition state.

As explained above, the data used by Tang *et al.*[25] for rate constant calculations are inconsistent with the results obtained using the applied methods. Thus, the rate constants of the maim channel pathways are calculated by the corrected energies. So, the rate constants for P1 and P2 generation pathways recalculated at the CCSD(T)/6-311++G(d,p)//B3LYP/6-311G(d,p) level (energies are obtained at the CCSD(T)/6-311++G(d,p)//B3LYP/6-311G(d,p) computational level and partition functions are taken at the B3LYP/6-311G(d,p) level). Theoretical rate constants obtained at this level using TST and VTST theories have large differences from observed rate constants experimentally by different groups, which are referred to below. Obtained rate constants at this level are collected in Tables S9-S11. The Shavit tunneling factor is considered for correcting high-pressure limit rate constants. The obtained rate constants of P1 adducts through the pathways 1 and 2 by TST theory at the UM06-2X/maTZ level in temperatures of 298.15, 400, and 600 K are 8.38×10^{-11}, 6.21×10^{-11}, and 6.27×10^{-11} cm^{-3} $molecule^{-1}$ s^{-1}, respectively. The mentioned rates using VTST theory are 7.31×10^{-11}, 5.49×10^{-11}, and 5.62×10^{-11} cm^{-3} $molecule^{-1}$ s^{-1}, respectively. At a high-level ab initio computation, the CCSD(T)/aTZ//MP2/aTZ level, rate constants of the considered adducts by using TST theory at the same temperatures are 2.11×10^{-10}, 7.26×10^{-11}, and 3.34×10^{-11} cm^{-3} $molecule^{-1}$ s^{-1}, respectively. Also, the obtained results using the VTST theory are 7.10×10^{-11}, 3.72×10^{-11}, and 2.52×10^{-11} cm^{-3} $molecule^{-1}$ s^{-1}, respectively. Our computed rate constants using TST and VTST theories at the UM06-2X/maTZ level have a good agreement with the experimentally reported rate constant by Vaghjiani[21] ($(6.50 \pm 1.3) \times 10^{-11}$ cm^3 $molecule^{-1}$ s^{-1}), which has independent temperature behavior. Also, our results have a good agreement with Harris *et al.*[23] results. Their reported rate constants using the

photolysis-resonance fluorescence technique at temperatures of 298.15 and 400 K were 6.69×10^{-11} and 5.84×10^{-11} cm^3 $molecule^{-1}$ s^{-1}, respectively. Our calculated rate constants at room temperature using TST and VTST theories at the CCSD(T)/aTZ//MP2/maTZ level are in excellent agreement with the experimental value (3.60×10^{-11} cm^3 $molecule^{-1}$ s^{-1}) reported by Vaghjiani[22]. Also, a good agreement is observed for overall rate constants of title reaction at room temperature by Hack *et al*.[24] (2.16×10^{-11} cm^3 $molecule^{-1}$ s^{-1}). The graphs that sketched by using the obtained rate constants theoretically and experimentally are brought in Figures 3a and 3b, respectively, for P1 adducts.

The rate constants of P2 adducts through the paths 3, 4, and 6 using TST theory at the UM06-2X/maTZ level in temperatures of 298.15, 400, 600, 1000, and 3000 K are 1.48×10^{-29}, 2.30×10^{-25}, 3.77×10^{-21}, 1.45×10^{-17}, and 2.60×10^{-13} cm^{-3} $molecule^{-1}$ s^{-1}, respectively. The rate constants for P3 adducts at the mentioned temperatures are 1.96×10^{-43}, 8.72×10^{-36}, 3.27×10^{-28}, 6.57×10^{-22}, and 8.38×10^{-15} cm^{-3} $molecule^{-1}$ s^{-1}, respectively. The rate constants for these adducts at several levels are computed and listed in Tables S11, S15-S18, and S24-S26 in the supplementary data. In summary, comparing the rate constant reported here with different experimental results shows that our used methods have adequately precise in describing the title reaction kinetics.

The low-pressure limit rate constant and its behavior in the falloff regime.

To investigate the pressure-dependent rate constant, the strong collision master equation Rice-Ramsperger-Kassel-Marcus (RRKM) theory is used. The rate constant of the title reaction in the low-pressure limit and its behavior in the falloff range is investigated in the 200-800 K temperature range. The chemical activation mechanism is implemented in the pressure-dependent rate constant as follows:

$$N_2H_4 + OH \xrightarrow{K(T)} Cr \qquad (1)$$

$$Cr + M \xrightarrow{k_1} Cr^* + M \qquad (2)$$

$$Cr^* + M \xrightarrow{k_{-1}} Cr + M \qquad (3)$$

$$Cr^* \xrightarrow{k_2} N_2H_3 + H_2O \qquad (4)$$

where M is the third body. If we apply the steady-state approximation to the concentration of Cr*, the rate of conversion of Cr to final adducts is

$$k_i(T,p) = \frac{k_1 k_2 [M]}{k_{-1}[M] + k_2} \qquad (1)$$

At high pressure limit ([M] → ∞), k(T,p) is the first order and at low-pressure limit (where [M] → 0) k(T,p) is the second order. Therefore, in the high and low-pressures, k(T,p) expressions in Eq.1 can be written as follows:

$$k_\infty = \frac{k_1 k_2}{k_{-1}} \qquad ([M] \to \infty) \qquad (2)$$

and

$$k_0 = k_1 [M] \qquad ([M] \to 0) \qquad (3)$$

If we divide the numerator and the denominator of equation 1 into k_{-1} [M] and substitute equations 2 and 3 in it, we have:

$$k_i(T,p) = \frac{k_\infty}{1 + \frac{k_\infty}{k_0}} \qquad (4)$$

Finally, for the calculation of pressure dependence of the rate constant, the following relation is used:

$$k(T,p) = \kappa K(T) k_i(T,p) \qquad (5)$$

where κ is tunneling correction, and *K(T)* is the temperature dependent equilibrium constant. Similar to temperature dependent rate constants, the Shavitt transmission coefficient was used for the correction of pressure-dependent rate constants. Because the nitrogen molecule is the most abundant species relative to other molecules in the atmosphere, it is used as the third body in the calculation of k(T,p). In the investigation of pressure effect on the temperature dependent rate constant by the master equation, the Lenard Jones parameters, σ (Å), and ε / k_B (K), and also the average amount of energy transferred per collision are important. The Lenard-Jones parameters of the reactants and bath gas are

4.230 Å and 250.000 K for N_2H_4, 2.750 Å, and 80.000 K for OH, and 3.798 Å and 71.400 K for N_2.[61] In the zero-pressure limit, $P \rightarrow 0$, $k(T,p)/[N_2]$ is called the low-pressure limit rate constant $k_0(T)$. $k_0(T)$ is a termolecular rate constant with the units of cm^6 $molecule^{-2}$ s^{-1} and also called pseudo third order rate constant. Our calculated rate constants at the low-pressure limit in the temperature range of 200-800K are listed in Table S29. The results show that $k_0(T)$ is 7.87×10^{-32}, 2.8×10^{-32}, and 1.09×10^{-32} cm^{-6} $molecule^{-2}$ s^{-1} at 298.15, 400 and 600 K, respectively. To our knowledge, the rate constant is not determined experimentally at the low-pressure limit for the generation of main reaction products.

Our calculated rate constants at different pressures in the falloff regime in the temperature range of 200-800K are depicted in figure 4 and collected in Table S29. By using equation 4, we concluded that the ratio of k_∞/k_0 is significant in the calculation of $k(T,p)$. The clear results relating to the effect of pressure on the main reaction pathways are seen when the pressure increases in the 200-800 K temperature range. In 298.15, 400, and 600 K, the ratio of k_∞/k_0 is 38.8, 196.0, and 513.0, respectively, which shows this ratio increases over the considered temperature range.

Reducing the calculated rate constants at 298.15 K into the rate constants at 1 bar, make better insight into the effect of pressure on the rate of reaction at room temperature. The reduced values of $k(T,p)/k(T,1\ bar)$ for $p=10^{-4}$, 0.01, 100, and 10^4 bar are 8.71×10^{-4}, 2.96×10^{-2}, 17.2, and 43.8 at 298.15 K, and 3.72×10^{-4}, 2.05×10^{-2}, 27.3, and 110 at 400 K, respectively. Our data show that the rate constant increases with increasing pressure in the 200-800 K temperature range.

Kinetic and thermodynamic viewpoints

Enthalpies and Gibbs free energies of all products calculated at the M06-2X/aQZ and MP2/aTZ levels in the temperature range of 200-1200 K are tabulated in Tables 4 and S31. The results show that among all the obtained products, P1 adducts are the most stable. Moreover, P2 adducts are more stable than P3. Based on the obtained results, the amount of stability of P1 products increases with the temperature that is going from -37.17 in 200 K to -41.45 kcal/mol in 1200 K.

According to the origin of Gibbs free energy and Table 4 information, the stability of P1 is related to the entropy of reaction that increases with temperature. The variation of $T\Delta S^\circ$ for P1 in the temperature range 200-1200 K equals 0.8-4.78 kcal/mol. The same behavior for the stability of P2 adducts is observed, but it is changed inversely for P3 adducts that relate to whose electronic entropy. With

increasing temperature from 200 to 1200 K, the amount of $T\Delta S^{\circ}$ for these species decreases from -1.88 to -6.86 kcal/mol. Another factor for the instability of P3 adducts is the enthalpy function by total variation about +2.53 kcal/mol that is related to the instability of the atom H. For P1 and P2 adducts, the variation of enthalpy is low in the mentioned temperature range.

In summary, with increasing temperature, the P1 and P2 generations are more favorable not only thermodynamically but also kinetically. The production of P3 adducts is favorable just kinetically at a temperature above 1000 K.

The fate of hydrazine in the atmosphere

The lifetimes of hydrazine in the atmosphere at altitudes from 0 to 50 km (corresponding to pressures from 1013 to 0.801 mbar) are listed in Tables 5, S7, and S8. The results show the H abstraction process is a key step for hydrazine degradation in the atmosphere. The computed rate constant decreases with increasing altitude from 2.83×10^{-12} to 3.52×10^{-14} cm^3 $molecule^{-1}s^{-1}$. Therefore, the calculated atmospheric lifetime of hydrazine degradation in the environment of hydroxyl radical varies from 32.8 to 1161.11 hours.

The tropospheric half-life of hydrazine in the reaction with hydroxyl radical was reported ~3 h by Harris *et al.*[23] By assuming roughly 1.1×10^6 molecule cm^{-3} for OH concentration, Vaghjiani[22] estimated that the fate of N_2H_4 is 6.6 hours at an average ambient temperature of 279 K. A difference is observed between our calculated lifetime with the results obtained by Vaghjiani and Harris *et al* experimentally. They have used the high-pressure limit rate constant instead of the pressure-dependent rate constant to calculate the mentioned half-life. Thus, If we use the obtained high-pressure limit rate constant by Hack[24] (2×10^{-11} cm^3 $molecule^{-1}$ s^{-1}) at 298 K with the OH concentration reported by Vaghjiani, the lifetime of N_2H_4 will be 12.6 hours. Our computed overall high-pressure limit rate constant for H abstraction channels is 8.39×10^{-11} cm^3 $molecule^{-1}$ s^{-1} at room temperature. If we use this value with the mentioned concentration for OH, the lifetime of hydrazine is 3.01 hours. Tuazon et al. have estimated an upper limit for the corresponding lifetime in the $N_2H_4 + O_3$ reaction. Their reported rate coefficient at 298 K is 1.4×10^{-16} cm^3 molecu1e^{-1} s^{-1}. They used concentration for O_3 in the atmosphere was about 5×10^{11} molecule cm^{-3} or less. Therefore, the obtained lifetime for N_2H_4 degradation was about 2.6 hours or longer[62]. As we know, the concentration of O_3 in the ozone layer is larger than the other parts of the atmosphere, and O_3 concentration is also less than the concentration

of OH radical in the urban area. Therefore, hydroxyl radical is an important factor for hydrazine degradation in urban areas.

Conclusion

The kinetics and mechanisms of the N_2H_4 + OH reaction, including reliable paths, are investigated by accurate quantum chemical methods. The results obtained by single reference methods such as B3LYP, M06-2X, MP2, and CCSD(T) in conjunction with augmented triple zeta basis sets (6-311++g(3df,3pd) and aTZ) show that there are small differences among the computed relative energies of all stationary points in the mentioned methods. The relative energies of the multi-reference method (MR-MP2) are different compared with the single-reference methods, which correspond to select of small active space for the N_2H_4 + OH case. Therefore, the sensitivity of the doublet PES of the title reaction for the applied methods and basis sets is negligible. The rate constant calculations show that sum of the first and second paths rate constants have negative temperature dependence behavior at low temperatures until 540 K at the M06-2X/maTZ level, and have positive temperature dependence behavior in the range of 560-3000 K. Our computed high-pressure limit rate constants using two formalisms, TST and VTST theories, show the results of DFT-M06-2X/maTZ level at low temperatures are roughly temperature independent, which have excellent agreement with the experimental results (see Figures 3a and 3b). Also, the same results computed by the CCSD(T) method along with several basis sets (on optimized structures of the MP2/aTZ level) at low temperatures depend on temperature. By applying pressure on the P1 generation pathways, we demonstrated that the reaction rate has a positive pressure dependence behavior. Finally, the variation of the rate constant with pressure is inversely related to temperature. Thermodynamic parameters of all suggested adducts are reported and discussed at the M06-2X/aQZ and MP2/aTZ levels. Some of the predicted adducts can be produced in the atmosphere with a wave number greater than 700 cm^{-1}.

Supporting information

See Supporting information for important geometrical parameters of the optimized structures, topological analysis of bond critical and ring critical points, unscaled vibrational frequencies, electronic, zero point, and relative energies. Also, the computed forward and reverse barrier heights, rate constants for all paths at different pressures and levels, Cartesian coordinates of optimized geometries in different levels, thermodynamic parameters at different levels, T1 diagnostic values, and the largest amplitudes.

Acknowledgments

This work was supported by University of Zanjan.

References

1 Clark, C. C. *Hydrazine*. (Mathieson Chemical Corporation, 1953).
2 Audrieth, L. F., Ogg, B. A. & Ackerson, B. *The chemistry of hydrazine*. (Wiley, 1951).
3 Byrkit, G. & Michalek, G. Hydrazine in organic chemistry. *Industrial & Engineering Chemistry* **42**, 1862-1875 (1950).
4 Gallant, R. PHYSICAL PROPERTIES OF HYDROCARBONS. 37. NITROGEN CONTAINING COMPOUNDS. *Hydrocarbon Processing* **48**, 117-& (1969).
5 Hudson, G. (Wiley, New York, 1967).
6 Syage, J. A., Cohen, R. B. & Steadman, J. Spectroscopy and dynamics of jet-cooled hydrazines and ammonia. I. Single-photon absorption and ionization spectra. *The Journal of chemical physics* **97**, 6072-6084 (1992).
7 Swaddle, T. W. *Applied inorganic chemistry*. (Univ of Calgary Pr, 1990).
8 Buxton, G. V. & Stuart, C. R. Radiation chemistry of aqueous solutions of hydrazine at elevated temperatures. Part 1.—Oxygen-free solutions. *Journal of the Chemical Society, Faraday Transactions* **92**, 1519-1525 (1996).
9 Schirmann, J. P. & Bourdauducq, P. Hydrazine. *Ullmann's Encyclopedia of Industrial Chemistry* (2000).
10 Rothgery, E. F. Hydrazine and its derivatives. *Kirk-Othmer Encyclopedia of Chemical Technology* (2000).
11 Choudhary, G. & Hansen, H. Human health perspective of environmental exposure to hydrazines: A review. *Chemosphere* **37**, 801-843 (1998).
12 Stone, D. A. Atmospheric chemistry of propellant vapors. *Toxicology letters* **49**, 349-360 (1989).
13 Sutton, G. P. *Rocket Propulsion Elements: An Introduction to the Engineering of Rockets*. (Wiley, 1963).
14 Liu, H. X. *et al.* CH3NHNH2+ OH reaction: Mechanism and dynamics studies. *Journal of computational chemistry* **30**, 2194-2204 (2009).
15 Sun, H., Zhang, P. & Law, C. K. Gas-Phase Kinetics Study of Reaction of OH Radical with CH3NHNH2 by Second-Order Multireference Perturbation Theory. *The Journal of Physical Chemistry A* **116**, 5045-5056 (2012).
16 Catoire, L., Chaumeix, N., Pichon, S. & Paillard, C. Visualizations of gas-phase NTO/MMH reactivity. *Journal of propulsion and power* **22**, 120-126 (2006).
17 Palaszewski, B., Ianovski, L. S. & Carrick, P. Propellant technologies: far-reaching benefits for aeronautical and space-vehicle propulsion. *Journal of Propulsion and Power* **14**, 641-648 (1998).
18 Masterton, W. L. & Hurley, C. N. *Chemistry: principles and reactions*. (Cengage Learning, 2015).
19 Thynell, S. *et al.* Spray and Combustion of Gelled Hypergolic Propellants for Future Rocket and Missile Engines. (PENNSYLVANIA STATE UNIV STATE COLLEGE, 2014).

20 Atkinson, R. A structure-activity relationship for the estimation of rate constants for the gas-phase reactions of OH radicals with organic compounds. *International journal of chemical kinetics* **19**, 799-828 (1987).
21 Vaghjiani, G. in *34th AIAA/ASME/SAE/ASEE Joint Propulsion Conference and Exhibit.* 3542.
22 Vaghjiani, G. L. Kinetics of OH reactions with N2H4, CH3NHNH2 and (CH3) 2NNH2 in the gas phase. *International Journal of Chemical Kinetics* **33**, 354-362 (2001).
23 Harris, G., Atkinson, R. & Pitts, J. Kinetics of the reactions of the hydroxyl radical with hydrazine and methylhydrazine. *Journal of Physical Chemistry* **83**, 2557-2559 (1979).
24 Hack, W., Hoyermann, K. & Wagner, H. G. Reaktionen des Hydroxylradikals mit Ammoniak und Hydrazin in der Gasphase. *Berichte der Bunsengesellschaft für physikalische Chemie* **78**, 386-391 (1974).
25 Tang, Y. *et al.* Mechanistic and kinetic investigations of N2H4+ OH reaction. *Journal of computational chemistry* **31**, 1520-1527 (2010).
26 Tuazon, E. C., Carter, W. P., Atkinson, R. & Pitts Jr, J. N. The gas-phase reaction of hydrazine and ozone: A nonphotolytic source of OH radicals for measurement of relative OH radical rate constants. *International Journal of Chemical Kinetics* **15**, 619-629 (1983).
27 Del Bene, J. E., Person, W. B. & Szczepaniak, K. Properties of Hydrogen-Bonded Complexes Obtained from the B3LYP Functional with 6-31G (d, p) and 6-31+ G (d, p) Basis Sets: Comparison with MP2/6-31+ G (d, p) Results and Experimental Data. *The Journal of Physical Chemistry* **99**, 10705-10707 (1995).
28 Anglada, J. M., Olivella, S. & Solé, A. Hydrogen transfer between sulfuric acid and hydroxyl radical in the gas phase: Competition among hydrogen atom transfer, proton-coupled electron-transfer, and double proton transfer. *The Journal of Physical Chemistry A* **110**, 1982-1990 (2006).
29 Basch, H. & Hoz, S. Ab initio study of hydrogen abstraction reactions. *The Journal of Physical Chemistry A* **101**, 4416-4431 (1997).
30 Feller, D., Peterson, K. A. & Grant Hill, J. On the effectiveness of CCSD (T) complete basis set extrapolations for atomization energies. *The Journal of chemical physics* **135**, 044102 (2011).
31 Møller, C. & Plesset, M. S. Note on an approximation treatment for many-electron systems. *Physical review* **46**, 618 (1934).
32 Becke, A. D. Becke's three parameter hybrid method using the LYP correlation functional. *J. Chem. Phys* **98**, 5648-5652 (1993).
33 Lee, C., Yang, W. & Parr, R. G. Development of the Colle-Salvetti correlation-energy formula into a functional of the electron density. *Physical review B* **37**, 785 (1988).
34 Papajak, E., Leverentz, H. R., Zheng, J. & Truhlar, D. G. Efficient Diffuse Basis Sets: cc-pV x Z+ and maug-cc-pV x Z. *Journal of chemical theory and computation* **5**, 1197-1202 (2009).
35 Dunning Jr, T. H. Gaussian basis sets for use in correlated molecular calculations. I. The atoms boron through neon and hydrogen. *The Journal of chemical physics* **90**, 1007-1023 (1989).
36 Zhao, Y. & Truhlar, D. G. The M06 suite of density functionals for main group thermochemistry, thermochemical kinetics, noncovalent interactions, excited states, and transition elements: two new functionals and systematic testing of four M06-class functionals and 12 other functionals. *Theoretical Chemistry Accounts* **120**, 215-241 (2008).
37 Zhao, Y. & Truhlar, D. G. Density functionals with broad applicability in chemistry. *Accounts of chemical research* **41**, 157-167 (2008).

38 Fukui, K. The path of chemical reactions-the IRC approach. *Accounts of chemical research* **14**, 363-368 (1981).
39 Ishida, K., Morokuma, K. & Komornicki, A. The intrinsic reaction coordinate. An abinitio calculation for HNC→ HCN and H−+ CH4→ CH4+ H−. *The Journal of Chemical Physics* **66**, 2153-2156 (1977).
40 Troya, D., Mosch, M. & O'Neill, K. A. Ab Initio and Dynamics Study of the O (3P)+ NH3 and O (3P)+ N2H4 Reactions at Hyperthermal Collision Energies. *The Journal of Physical Chemistry A* **113**, 13863-13870 (2009).
41 Spada, R. F. *et al.* Hydrogen abstraction from the hydrazine molecule by an oxygen atom. *The Journal of Physical Chemistry A* **119**, 1628-1635 (2015).
42 Spada, R. F., Ferrão, L. F., Roberto-Neto, O., Lischka, H. & Machado, F. B. Thermochemical and kinetics of hydrazine dehydrogenation by an oxygen atom in hydrazine-rich systems: A dimer model. *The Journal of Physical Chemistry A* **119**, 12607-12614 (2015).
43 Riley, K. E. & Hobza, P. Assessment of the MP2 method, along with several basis sets, for the computation of interaction energies of biologically relevant hydrogen bonded and dispersion bound complexes. *The Journal of Physical Chemistry A* **111**, 8257-8263 (2007).
44 Grabowski, S. J. *Hydrogen bonding: new insights*. Vol. 3 (Springer, 2006).
45 Halkier, A. *et al.* Basis-set convergence in correlated calculations on Ne, N2, and H2O. *Chemical Physics Letters* **286**, 243-252 (1998).
46 Hirao, K. Multireference Møller—Plesset method. *Chemical physics letters* **190**, 374-380 (1992).
47 Hirao, K. Multireference Møller—Plesset perturbation theory for high-spin open-shell systems. *Chemical physics letters* **196**, 397-403 (1992).
48 Lee, T. J. & Taylor, P. R. A diagnostic for determining the quality of single-reference electron correlation methods. *International Journal of Quantum Chemistry* **36**, 199-207 (1989).
49 Raghavachari, K., Trucks, G. W., Pople, J. A. & Head-Gordon, M. A fifth-order perturbation comparison of electron correlation theories. *Chemical Physics Letters* **157**, 479-483 (1989).
50 Rienstra-Kiracofe, J. C., Allen, W. D. & Schaefer, H. F. The C2H5+ O2 reaction mechanism: high-level ab initio characterizations. *J. Phys. Chem. A* **104**, 9823-9840 (2000).
51 Peiró-García, J., Nebot-Gil, I. & Merchán, M. An ab initio study on the mechanism of the atmospheric reaction NH2+ O3→ H2NO+ O2. *ChemPhysChem.* **4**, 366-372 (2003).
52 Lambert, N., Kaltsoyannis, N., Price, S. D., Žabka, J. & Herman, Z. Bond-Forming Reactions of Dications with Molecules: A Computational and Experimental Study of the Mechanisms for the Formation of HCF2+ from CF32+ and H2. *J. Phys. Chem. A* **110**, 2898-2905 (2006).
53 Biegler-König, F., Schönbohm, J., Derdau, R., Bayles, D. & Bader, R. AIM2000, version 2.0. *McMaster University* (2002).
54 Frisch, M. *et al.* (Gaussian, Inc., Wallingford CT, 2009).
55 Roy, D., Todd, A. & John, M. Gauss View 5.0. 8. *Gaussian, Wallingford, Conn, USA* (2009).
56 Eyring, H. The activated complex in chemical reactions. *The Journal of Chemical Physics* **3**, 107-115 (1935).
57 Bao, J. L. & Truhlar, D. G. Variational transition state theory: theoretical framework and recent developments. *Chemical Society Reviews* **46**, 7548-7596 (2017).
58 Miyoshi, A. Gaussian post processor (GPOP). *University of Tokyo, Tokyo* (2010).
59 Miyoshi, A. Steady-state unimolecular master-equation solver (SSUMES). *University of Tokyo* (2010).

60 Shavitt, I. A Calculation of the Rates of the Ortho-Para Conversions and Isotope Exchanges in Hydrogen. *The Journal of Chemical Physics* **31**, 1359-1367 (1959).
61 Kee, R. *et al.* Transport: a software package for the evaluation of gas-phase, multicomponent transport properties. *Chemkin Collection* (1999).
62 Tuazon, E. C., Carter, W. P., Winer, A. M. & Pitts, J. N. Reactions of hydrazines with ozone under simulated atmospheric conditions. *Environmental Science & Technology* **15**, 823-828 (1981).
63 Long, B., Bao, J. L. & Truhlar, D. G. Reaction of SO 2 with OH in the atmosphere. *Physical Chemistry Chemical Physics* **19**, 8091-8100 (2017).

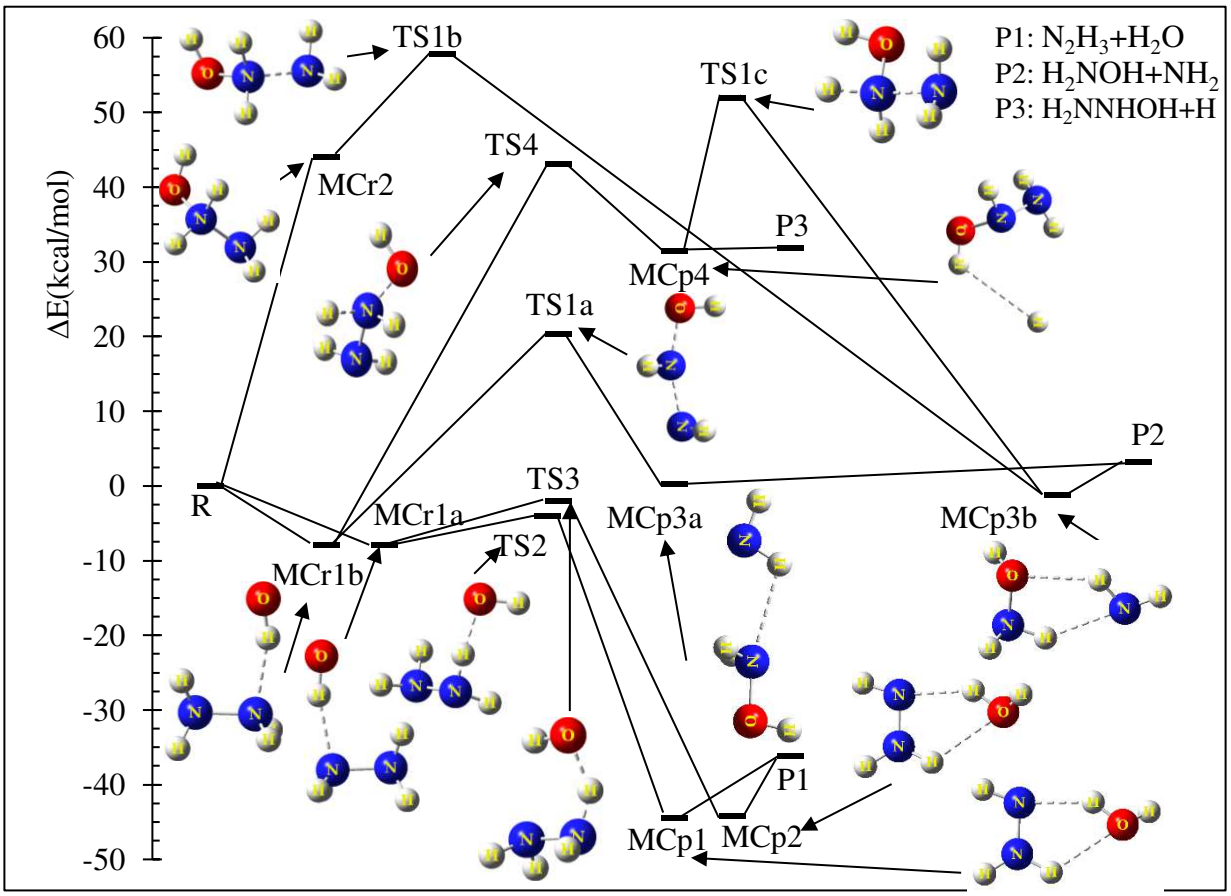

Figure 1. Potential energy profile of the N_2H_4 + OH reaction for reliable pathways at the CCSD(T)/CBS//MP2/aTZ level.

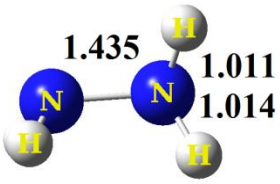

N_2H_4

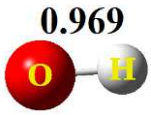

OH

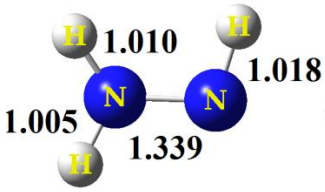

N_2H_3

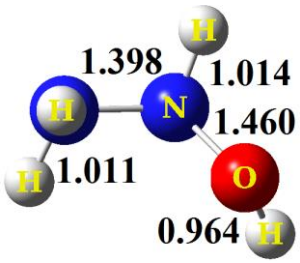

H_2NNH0H

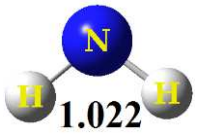

NH_2

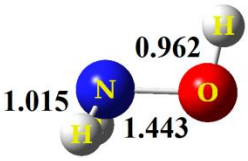

H_2NOH

H

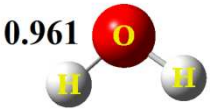

H_2O

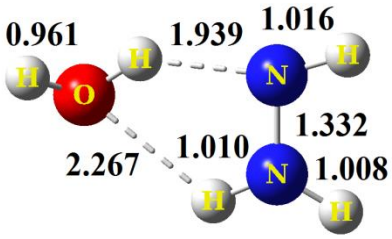

MCp1

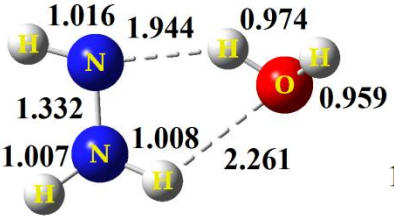

MCp2

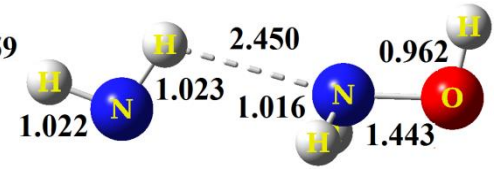

MCp3a

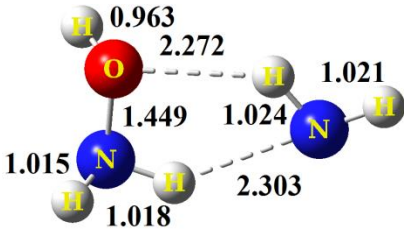

MCP3b

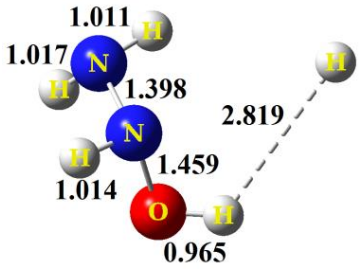

MCp4

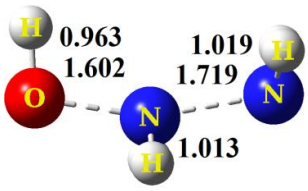

TS1

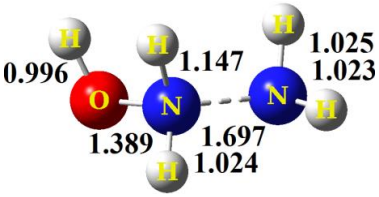

TS1b

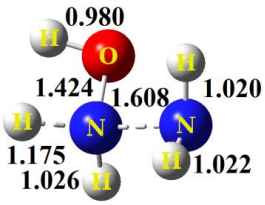

TS1c

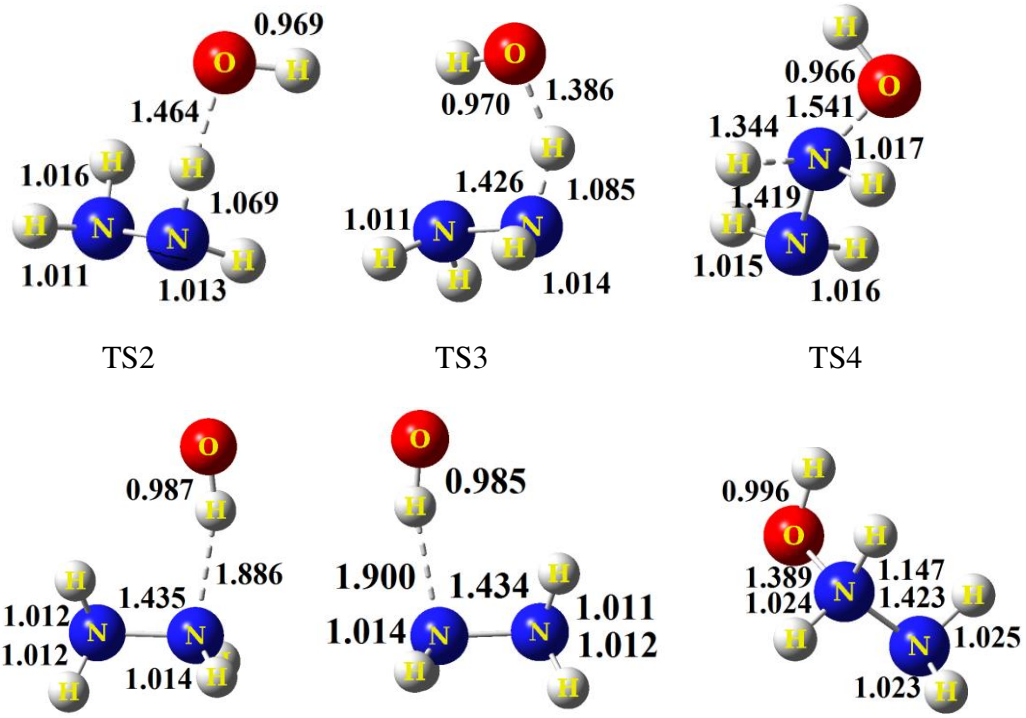

Figure 2. The optimized structural parameters of all species for reliable paths at the MP2/aTZ level.

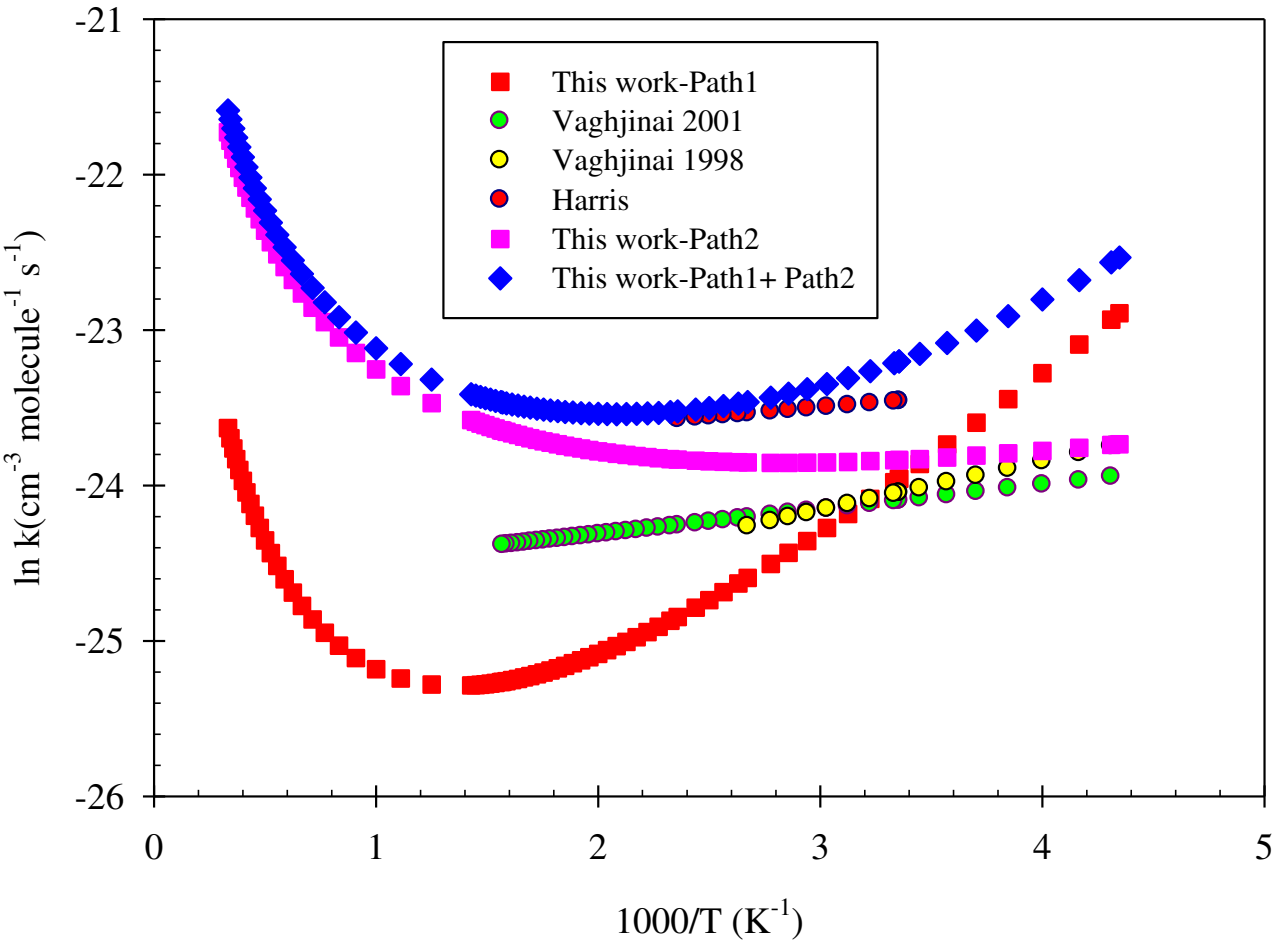

Figure 3a. Representation of Arrhenius plot for P1 production pathways by TST theory at the M06-2X/maTZ level.

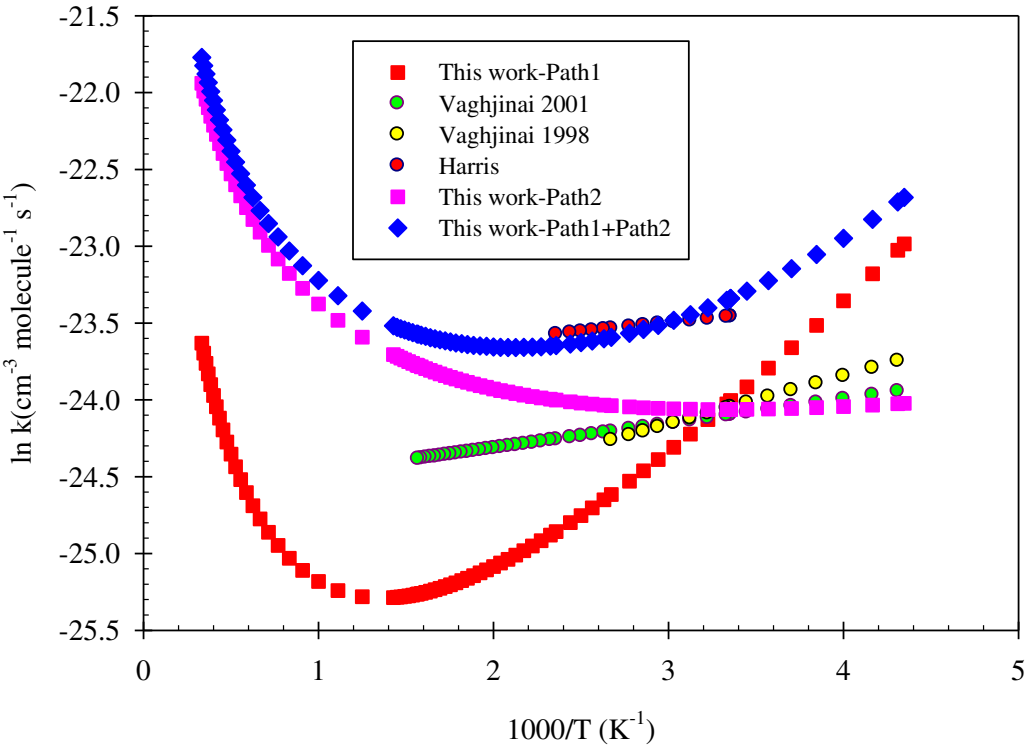

Figure 3b. Representation of Arrhenius plot for P1 production pathways by VTST theory at the M06-2X/maTZ level.

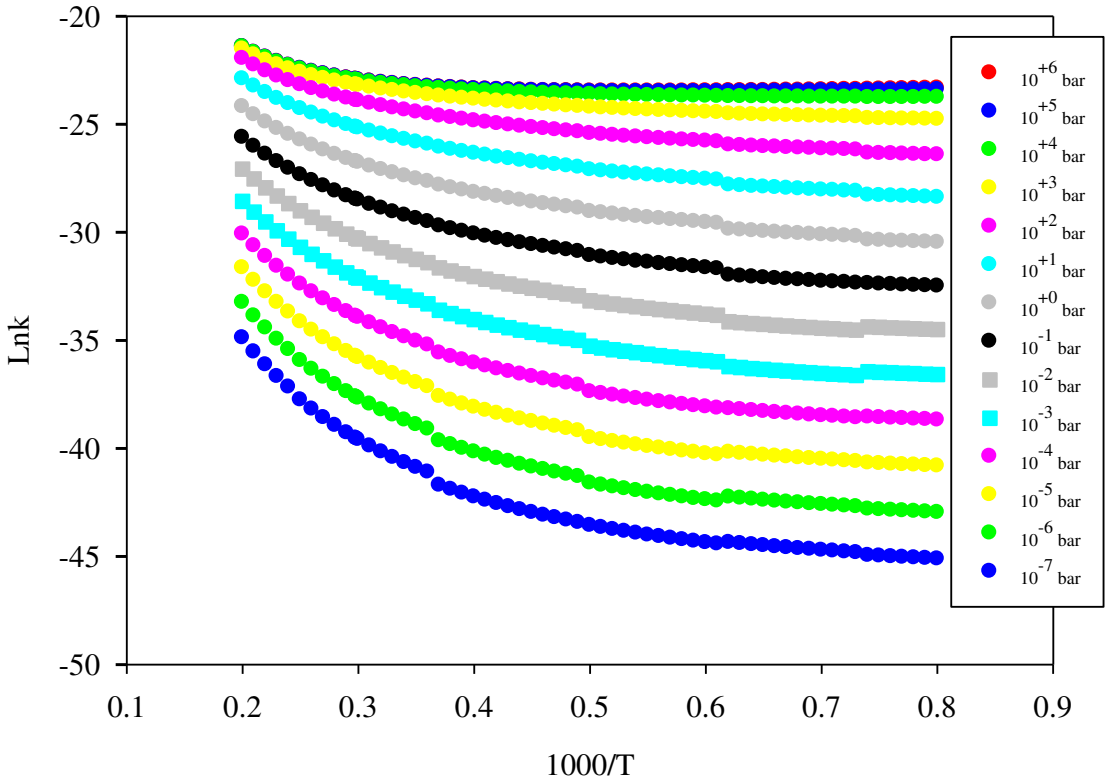

Figure 4. Representation of temperature and pressure-dependent rate constant of P1 production pathways (path 1 + path 2) of the N_2H_4 + OH reaction.

	TS2		TS3	
Method	N-H	H-O	N-H	H-O
MP2/aTZ	1.069	1.464	1.087	1.386
MP2/maTZ	1.068	1.463	1.085	1.386
M06-2X/aTZ	1.031	1.742	1.047	1.580
M06-2X /maTZ	1.031	1.751	1.040	1.626
M06-HF/aTZ	1.045	1.562	1.064	1.466
M06-HF /maTZ	1.046	1.563	1.064	1.466
B3LYP/aTZ	1.034	1.700	1.023	1.809
B3LYP/maTZ	1.035	1.693	1.023	1.808

Table 1. Bond lengths (in Å) for TS2 and TS3.

Species	E_{elec}	ΔE	$\Delta E_f^{\neq}$	$\Delta E_r^{\neq}$
R (N_2H_4+OH)	-187.44049	0.00		
MCr1a	-187.45305	-7.88		
MCr2	-187.37037	44.00		
TS1	-187.40797	20.41	28.29	20.20
TS1b	-187.34829	57.86	13.86	59.08
TS1c	-187.35757	52.03	59.91	20.61
TS2	-187.44540	-3.08	4.80	41.37
TS3	-187.44430	-2.39	5.49	41.87
TS4	-187.37169	43.17	51.05	11.75
MCp1	-187.51133	-44.45		
MCp2	-187.51103	-44.26		
MCp3a	-187.44016	0.21		
MCp3b	-187.44244	-1.22		
MCp4	-187.39042	31.42		
P1(N_2H_3+H_2O)	-187.49810	-36.15		
P2(NH_2+H_2NOH)	-187.43537	3.21		
P3(H_2NNHOH+OH)	-187.38978	31.82		

Table 2. The electronic energies (in Hartree), relative energies (ΔE) (in kcal mol^{-1}), forward barriers heights ($\Delta E_f^{\neq}$) (in kcal mol^{-1}), and reverse barrier heights ($\Delta E_r^{\neq}$) (in kcal mol^{-1}) of the reliable paths of N_2H_4 + OH reactions at the CCSD(T)/CBS level.

T/K	k^{TSTa}	k^{CVTa}	k^{TSTb}	k^{CVTb}	Sh-Corr[c]
230	1.64E-10	1.41E-10	8.51E-10	1.74E-10	43.09
232	1.59E-10	1.37E-10	8.06E-10	1.68E-10	42.72
240	1.41E-10	1.22E-10	6.55E-10	1.46E-10	41.32
250	1.25E-10	1.08E-10	5.16E-10	1.26E-10	39.69
260	1.12E-10	9.72E-11	4.15E-10	1.09E-10	38.19
270	1.02E-10	8.87E-11	3.40E-10	9.60E-11	36.80
280	9.44E-11	8.20E-11	2.83E-10	8.55E-11	35.51
290	8.80E-11	7.66E-11	2.40E-10	7.69E-11	34.31
298	8.39E-11	7.31E-11	2.11E-10	7.11E-11	33.40
298.15	8.38E-11	7.30E-11	2.11E-10	7.10E-11	33.39
300	8.29E-11	7.22E-11	2.05E-10	6.98E-11	33.19
310	7.88E-11	6.87E-11	1.78E-10	6.38E-11	32.14
320	7.53E-11	6.57E-11	1.56E-10	5.88E-11	31.16
330	7.25E-11	6.33E-11	1.38E-10	5.46E-11	30.24
340	7.01E-11	6.13E-11	1.23E-10	5.09E-11	29.37
350	6.81E-11	5.97E-11	1.11E-10	4.78E-11	28.56
360	6.64E-11	5.82E-11	1.01E-10	4.51E-11	27.78
374	6.46E-11	5.67E-11	8.89E-11	4.19E-11	26.78
380	6.39E-11	5.62E-11	8.46E-11	4.07E-11	26.37
390	6.29E-11	5.54E-11	7.82E-11	3.88E-11	25.71
400	6.21E-11	5.48E-11	7.26E-11	3.72E-11	25.09
410	6.15E-11	5.43E-11	6.78E-11	3.58E-11	24.50
424	6.08E-11	5.37E-11	6.21E-11	3.41E-11	23.72
430	6.05E-11	5.36E-11	5.99E-11	3.34E-11	23.40
440	6.02E-11	5.33E-11	5.67E-11	3.24E-11	22.89
450	6.00E-11	5.32E-11	5.38E-11	3.15E-11	22.40
460	5.98E-11	5.31E-11	5.12E-11	3.07E-11	21.93
470	5.97E-11	5.30E-11	4.9E-11	3.00E-11	21.48
480	5.97E-11	5.31E-11	4.69E-11	2.94E-11	21.05
490	5.97E-11	5.32E-11	4.51E-11	2.88E-11	20.64
500	5.98E-11	5.33E-11	4.34E-11	2.82E-11	20.25
510	5.99E-11	5.35E-11	4.19E-11	2.78E-11	19.87
520	6.01E-11	5.36E-11	4.06E-11	2.73E-11	19.50
530	6.03E-11	5.38E-11	3.93E-11	2.70E-11	19.15
540	6.06E-11	5.41E-11	3.82E-11	2.66E-11	18.81
550	6.08E-11	5.44E-11	3.72E-11	2.63E-11	18.49
560	6.12E-11	5.47E-11	3.63E-11	2.60E-11	18.18
570	6.15E-11	5.50E-11	3.55E-11	2.58E-11	17.87
580	6.19E-11	5.54E-11	3.47E-11	2.55E-11	17.58
590	6.22E-11	5.58E-11	3.40E-11	2.53E-11	17.30
600	6.27E-11	5.62E-11	3.34E-11	2.52E-11	17.03
610	6.31E-11	5.66E-11	3.28E-11	2.50E-11	16.76
620	6.36E-11	5.71E-11	3.23E-11	2.49E-11	16.51
630	6.40E-11	5.75E-11	3.18E-11	2.47E-11	16.26
637	6.44E-11	5.79E-11	3.15E-11	2.46E-11	16.09

640	6.45E-11	5.80E-11	3.13E-11	2.46E-11	16.02
650	6.50E-11	5.85E-11	3.09E-11	2.45E-11	15.79
660	6.56E-11	5.89E-11	3.06E-11	2.44E-11	15.56
670	6.61E-11	5.95E-11	3.02E-11	2.43E-11	15.35
680	6.67E-11	6.00E-11	2.99E-11	2.42E-11	15.13
690	6.73E-11	6.05E-11	2.96E-11	2.42E-11	14.93
700	6.79E-11	6.11E-11	2.94E-11	2.41E-11	14.73
800	7.46E-11	6.73E-11	2.80E-11	2.44E-11	13.01
900	8.25E-11	7.43E-11	2.81E-11	2.54E-11	11.67
1000	9.13E-11	8.21E-11	2.90E-11	2.71E-11	10.60
1100	1.01E-10	9.04E-11	3.06E-11	2.91E-11	9.72
1200	1.11E-10	9.95E-11	3.27E-11	3.16E-11	9.00
1300	1.23E-10	1.09E-10	3.52E-11	3.43E-11	8.38
1400	1.34E-10	1.19E-10	3.81E-11	3.74E-11	7.85
1500	1.47E-10	1.29E-10	4.13E-11	4.08E-11	7.39
1600	1.61E-10	1.41E-10	4.49E-11	4.45E-11	6.99
1700	1.75E-10	1.53E-10	4.89E-11	4.85E-11	6.64
1800	1.89E-10	1.64E-10	5.32E-11	5.28E-11	6.33
1900	2.05E-10	1.77E-10	5.78E-11	5.74E-11	6.05
2000	2.21E-10	1.91E-10	6.27E-11	6.23E-11	5.79
2100	2.38E-10	2.05E-10	6.80E-11	6.75E-11	5.57
2200	2.55E-10	2.19E-10	7.36E-11	7.29E-11	5.36
2300	2.74E-10	2.34E-10	7.96E-11	7.87E-11	5.17
2400	2.93E-10	2.49E-10	8.59E-11	8.48E-11	4.99
2500	3.12E-10	2.65E-10	9.26E-11	9.12E-11	4.83
2600	3.33E-10	2.81E-10	9.96E-11	9.79E-11	4.69
2700	3.54E-10	2.98E-10	1.07E-10	1.05E-10	4.55
2800	3.75E-10	3.15E-10	1.15E-10	1.12E-10	4.42
2900	3.98E-10	3.32E-10	1.23E-10	1.20E-10	4.30
3000	4.21E-10	3.51E-10	1.31E-10	1.28E-10	4.19

All of the rate constants are in $cm^3molecule^{-1}$ s^{-1}.

[a]calculated rate constant of P1 pathways at the M06-2X/maTZ with Shavit correction.

[b]calculated rate constant of P1 pathways at the CCSD(T)/aTZ//MP2/aTZ with Shavit correction.

[c]Shavit tunneling correction computed at the M06-2X/maTZ.

Table 3a. The high-pressure limit rate constants of P1 generation pathways (path 1 + path 2) and Shavitt tunneling correction.

T/K	k^{TSTa}	k^{CVTa}	k^{TSTb}	k^{CVTb}
230	2.29E-34	2.58E-34	2.70E-52	1.09E-52
232	3.47E-34	3.90E-34	5.82E-52	2.38E-52
240	1.71E-33	1.92E-33	1.11E-50	4.68E-51
250	1.09E-32	1.22E-32	3.40E-49	1.48E-49
260	6.07E-32	6.73E-32	7.99E-48	3.60E-48
270	2.97E-31	3.28E-31	1.49E-46	6.90E-47
280	1.30E-30	1.43E-30	2.25E-45	1.07E-45
290	5.16E-30	5.66E-30	2.83E-44	1.38E-44
298	1.45E-29	1.59E-29	1.90E-43	9.44E-44
298.15	1.48E-29	1.62E-29	1.96E-43	9.77E-44
300	1.87E-29	2.04E-29	3.00E-43	1.50E-43
310	6.24E-29	6.81E-29	2.74E-42	1.40E-42
320	1.94E-28	2.11E-28	2.18E-41	1.14E-41
330	5.63E-28	6.11E-28	1.53E-40	8.14E-41
340	1.54E-27	1.67E-27	9.61E-40	5.20E-40
350	3.98E-27	4.3E-27	5.43E-39	2.99E-39
360	9.77E-27	1.05E-26	2.79E-38	1.56E-38
374	3.18E-26	3.42E-26	2.39E-37	1.36E-37
380	5.14E-26	5.52E-26	5.73E-37	3.29E-37
390	1.11E-25	1.19E-25	2.31E-36	1.35E-36
400	2.3E-25	2.47E-25	8.72E-36	5.14E-36
410	4.63E-25	4.94E-25	3.09E-35	1.84E-35
424	1.17E-24	1.24E-24	1.64E-34	9.94E-35
430	1.70E-24	1.81E-24	3.25E-34	1.98E-34
440	3.13E-24	3.32E-24	9.76E-34	6.01E-34
450	5.6E-24	5.94E-24	2.79E-33	1.73E-33
460	9.78E-24	1.04E-23	7.64E-33	4.79E-33
470	1.67E-23	1.77E-23	2.00E-32	1.27E-32
480	2.8E-23	2.96E-23	5.06E-32	3.23E-32
490	4.59E-23	4.85E-23	1.23E-31	7.91E-32
500	7.39E-23	7.80E-23	2.89E-31	1.87E-31
510	1.17E-22	1.23E-22	6.59E-31	4.29E-31
520	1.82E-22	1.91E-22	1.45E-30	9.54E-31
530	2.78E-22	2.93E-22	3.12E-30	2.06E-30
540	4.2E-22	4.41E-22	6.50E-30	4.32E-30
550	6.24E-22	6.56E-22	1.32E-29	8.84E-30
560	9.16E-22	9.62E-22	2.62E-29	1.77E-29
570	1.33E-21	1.39E-21	5.09E-29	3.44E-29
580	1.90E-21	1.99E-21	9.65E-29	6.56E-29
590	2.69E-21	2.82E-21	1.79E-28	1.23E-28
600	3.77E-21	3.95E-21	3.27E-28	2.24E-28
610	5.23E-21	5.46E-21	5.84E-28	4.03E-28
620	7.18E-21	7.50E-21	1.02E-27	7.10E-28
630	9.76E-21	1.02E-20	1.77E-27	1.23E-27
637	1.20E-20	1.26E-20	2.57E-27	1.79E-27

640	1.31E-20	1.37E-20	3.00E-27	2.10E-27
650	1.76E-20	1.83E-20	5.02E-27	3.52E-27
660	2.33E-20	2.43E-20	8.27E-27	5.82E-27
670	3.06E-20	3.19E-20	1.34E-26	9.49E-27
680	4.00E-20	4.16E-20	2.15E-26	1.53E-26
690	5.18E-20	5.39E-20	3.40E-26	2.42E-26
700	6.67E-20	6.93E-20	5.31E-26	3.80E-26
800	6.03E-19	6.24E-19	2.56E-24	1.88E-24
900	3.47E-18	3.58E-18	5.47E-23	4.10E-23
1000	1.45E-17	1.49E-17	6.57E-22	5.00E-22
1100	4.79E-17	4.91E-17	5.17E-21	3.98E-21
1200	1.32E-16	1.35E-16	2.96E-20	2.30E-20
1300	3.17E-16	3.24E-16	1.32E-19	1.03E-19
1400	6.81E-16	6.95E-16	4.85E-19	3.81E-19
1500	1.34E-15	1.36E-15	1.52E-18	1.20E-18
1600	2.44E-15	2.48E-15	4.18E-18	3.31E-18
1700	4.19E-15	4.26E-15	1.03E-17	8.21E-18
1800	6.84E-15	6.94E-15	2.33E-17	1.86E-17
1900	1.07E-14	1.08E-14	4.87E-17	3.88E-17
2000	1.60E-14	1.62E-14	9.53E-17	7.61E-17
2100	2.33E-14	2.36E-14	1.76E-16	1.41E-16
2200	3.29E-14	3.33E-14	3.09E-16	2.48E-16
2300	4.54E-14	4.59E-14	5.21E-16	4.17E-16
2400	6.12E-14	6.19E-14	8.44E-16	6.76E-16
2500	8.09E-14	8.17E-14	1.32E-15	1.06E-15
2600	1.05E-13	1.06E-13	2.01E-15	1.61E-15
2700	1.34E-13	1.35E-13	2.97E-15	2.38E-15
2800	1.69E-13	1.71E-13	4.29E-15	3.44E-15
2900	2.11E-13	2.13E-13	6.05E-15	4.85E-15
3000	2.60E-13	2.62E-13	8.38E-15	6.71E-15

All of the rate constants are in $cm^3molecule^{-1}\ s^{-1}$.

[a]calculated rate constant of P2 pathways at the M06-2X/maTZ with Shavit correction.

[b]calculated rate constant of P3 pathways at the M06-2X/maTZ with Shavit correction.

Table 3b. The high-pressure limit rate constants of P2 and P3 generation pathways and Shavit tunneling correction.

R → P1(N_2H_3+H_2O)									
T/K	ΔE_T^0	ΔH_T^0	ΔG_T^0	$T\Delta S_T^0$	T/K	ΔE_T^0	ΔH_T^0	ΔG_T^0	$T\Delta S_T^0$
200	-36.37	-36.37	-37.17	0.80	500	-36.24	-36.24	-38.47	2.23
250	-36.33	-36.33	-37.37	1.04	550	-36.24	-36.25	-38.69	2.45
300	-36.30	-36.30	-37.59	1.29	600	-36.26	-36.26	-38.92	2.66
350	-36.27	-36.27	-37.80	1.54	700	-36.29	-36.29	-39.36	3.06
400	-36.25	-36.25	-38.03	1.77	900	-36.41	-36.41	-40.22	3.80
450	-36.24	-36.24	-38.25	2.01	1200	-36.67	-36.67	-41.45	4.78
R → P2(NH_2OH+NH_2)									
T/K	ΔE_T^0	ΔH_T^0	ΔG_T^0	$T\Delta S_T^0$	T/K	ΔE_T^0	ΔH_T^0	ΔG_T^0	$T\Delta S_T^0$
200	2.95	2.95	2.04	0.90	500	2.99	2.99	0.63	2.36
250	2.98	2.98	1.81	1.6	550	2.97	2.97	0.39	2.58
300	3.00	3.00	1.58	1.42	600	2.95	2.95	0.16	2.79
350	3.01	3.01	1.34	1.67	700	2.89	2.89	38.22	3.20
400	3.01	3.01	1.10	1.91	900	2.77	2.77	-1.20	3.97
450	3.00	3.00	0.87	2.14	1200	2.55	2.55	-2.49	5.04
R → P3(NH_2NHOH+H)									
T/K	ΔE_T^0	ΔH_T^0	ΔG_T^0	$T\Delta S_T^0$	T/K	ΔE_T^0	ΔH_T^0	ΔG_T^0	$T\Delta S_T^0$
200	27.80	27.80	29.68	-1.88	500	28.21	28.21	32.38	-4.17
250	27.81	27.81	30.15	-2.34	550	28.33	28.33	32.79	-4.45
300	27.85	27.85	30.61	-2.76	600	28.47	28.47	33.18	-4.71
350	27.91	27.91	31.07	-3.16	700	28.76	28.76	33.95	-5.19
400	27.99	27.99	31.51	-3.52	900	29.38	29.38	35.35	-5.97
450	28.09	28.09	31.95	-3.85	1200	30.33	30.33	37.20	-6.86

Table 4. The thermodynamic parameters (kcal/mol) of P1-P3 adducts of N_2H_4+ OH reaction on the doublet potential energy surface at the UM06-2X/aug-cc-pVQZ level.

H/km	*T*/K	*P*/mbar	k^b	[OH]/molecule cm^{-3}	τ^c/s	$\frac{k_\infty}{k}$
0	290.2	1013	2.83E-12	3.00E+06	1.18E+05	4.14E+01
5	250.2	495.9	4.03E-12	1.00E+06	2.48E+05	4.46E+01
10	215.6	242.8	7.17E-12	5.70E+05	2.45E+05	3.70E+01
15	198.0	118.8	9.12E-12	4.20E+05	2.61E+05	7.28E+01
20	208.0	58.18	3.80E-12	3.70E+05	7.11E+05	1.27E+02
25	216.1	28.48	1.73E-12	6.60E+05	8.78E+05	1.91E+02
30	221.5	13.94	8.66E-13	1.60E+06	7.22E+05	3.42E+02
35	228.1	6.826	4.13E-13	3.70E+06	6.54E+05	6.28E+02
40	240.5	3.341	1.60E-13	6.80E+06	9.21E+05	1.31E+03
45	251.9	1.636	6.34E-14	8.50E+06	1.86E+06	2.78E+03
50	253.7	0.801	3.52E-14	6.80E+06	4.18E+06	4.90E+03

[a] The altitude (H), pressure (P), the temperature (T), and the OH concentration ([OH]) in this Table are from reference[63].

[b] k is the bimolecular rate constant at the mentioned temperature and pressure.

[c] $\tau = \frac{1}{k[OH]}$ is the lifetime of N_2H_4 in the atmospheric concentration of OH.

Table 5. The rate constant of the N_2H_4 + OH reaction for Path 1+ Path 2, the concentration of hydroxyl radical in different altitudes, and lifetimes of N_2H_4 in the atmosphere in an ambient of atmospheric hydroxyl radical as functions of Height[a].

Author contributions

Hamed Douroudgari and Fahime Khouini performed calculations; Hamed Douroudgar analysed data, wrote the paper, and revised the manuscript; Morteza Vahedpour corrected the manuscript, reviewed the revised manuscript, and supervised the whole study.

Competing interests

The authors declare no competing interests.

Figures

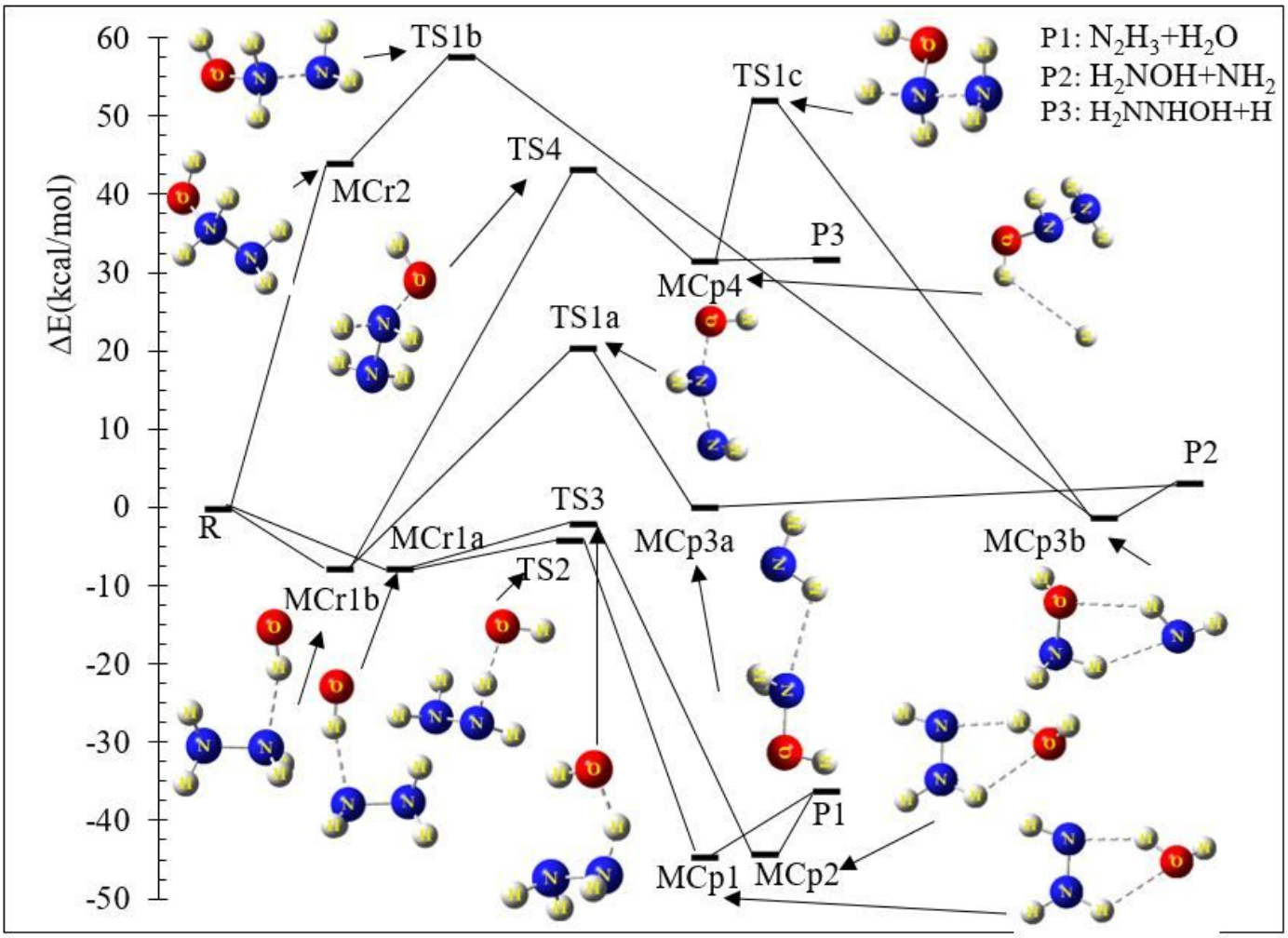

Figure 1

Potential energy profile of the N2H4 + OH reaction for reliable pathways at the CCSD(T)/CBS//MP2/aTZ level.

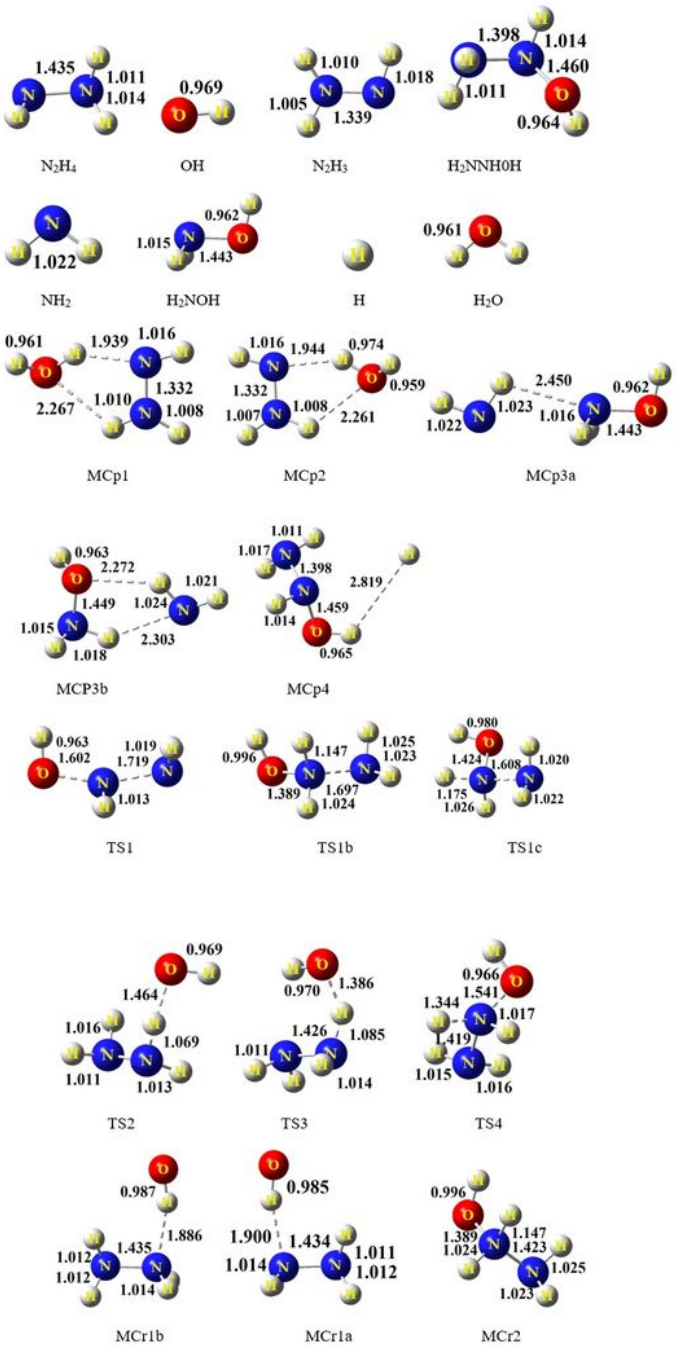

Figure 2

The optimized structural parameters of all species for reliable paths at the MP2/aTZ level.

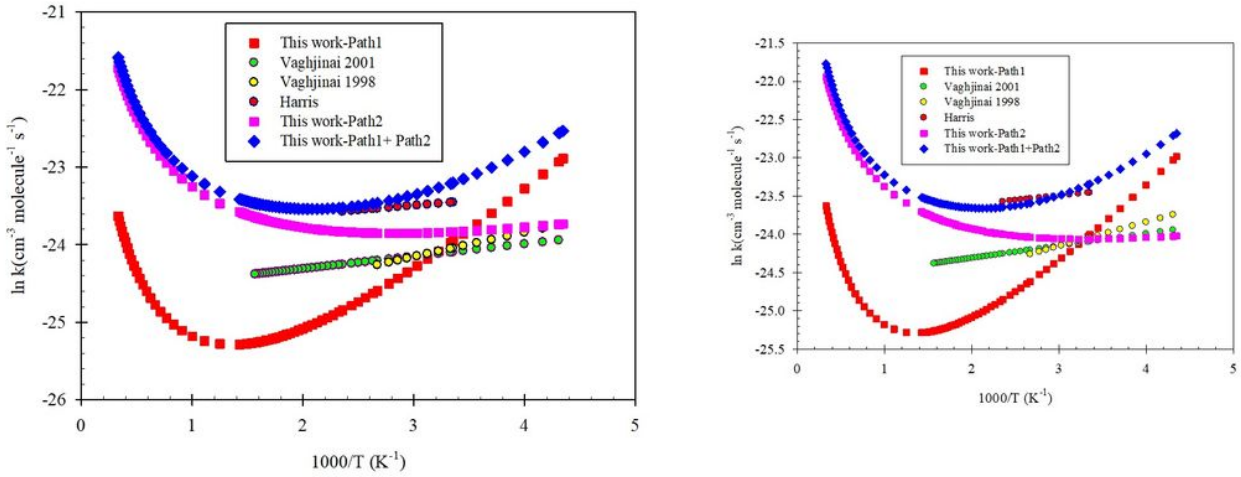

Figure 3

a. Representation of Arrhenius plot for P1 production pathways by TST theory at the M06-2X/maTZ level.
b. Representation of Arrhenius plot for P1 production pathways by VTST theory at the M06-2X/maTZ level.

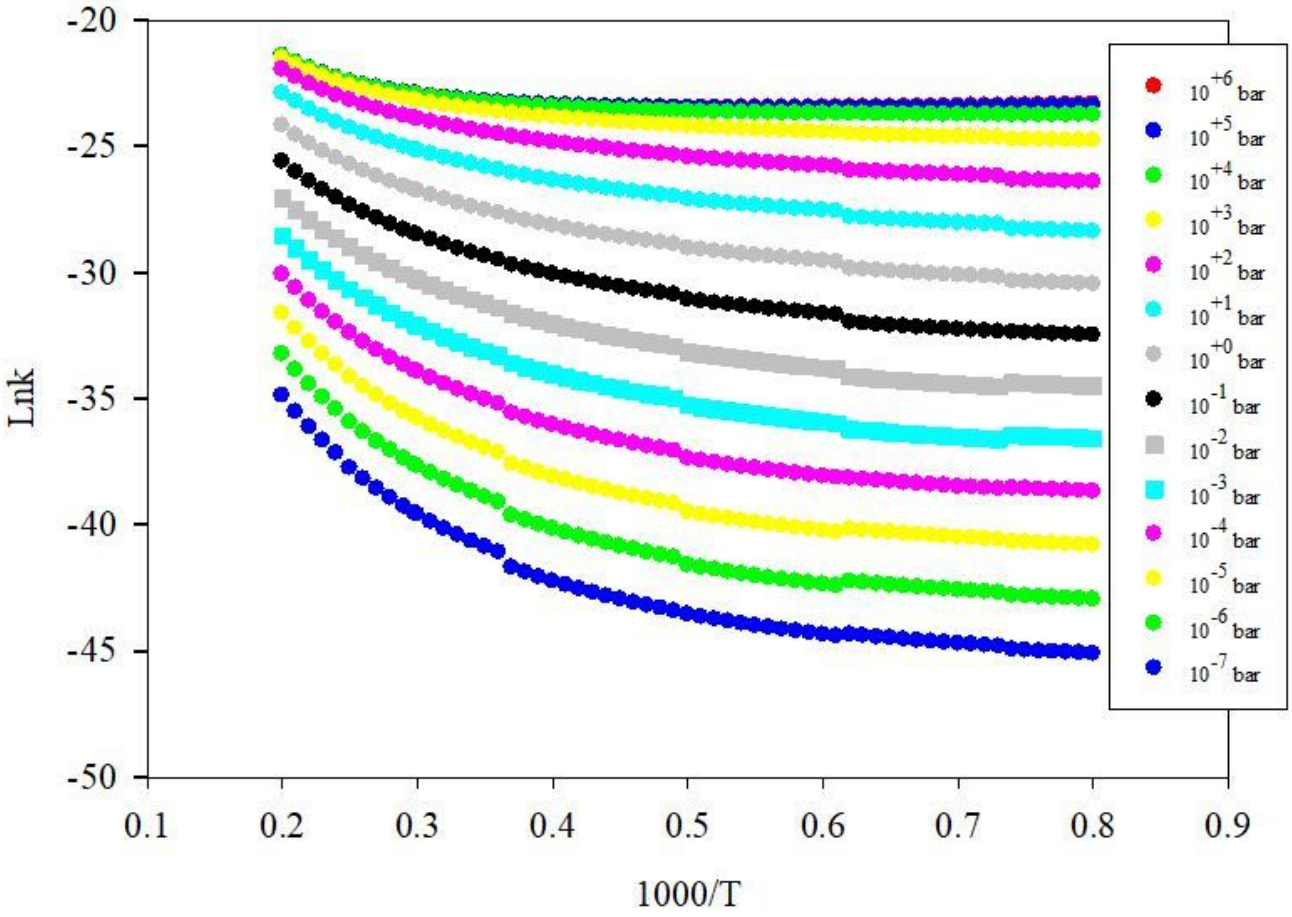

Figure 4

Representation of temperature and pressure-dependent rate constant of P1 production pathways (path 1 + path 2) of the N2H4 + OH reaction.

Supplementary Files

This is a list of supplementary files associated with this preprint. Click to download.

- SupportinginformationFourthRevisionClean.docx